2011

H2O contents in olivine-hosted melt inclusions from primitive magmas in the Northern Cascade arc

Steven D. Shaw
Western Washington University

H_2O CONTENTS IN OLIVINE-HOSTED MELT INCLUSIONS FROM PRIMITIVE MAGMAS IN THE NORTHERN CASCADE ARC

By

Steven D. Shaw

Accepted in Partial Completion
Of the Requirements for the Degree
Master of Science

Moheb A. Ghali, Dean of the Graduate School

ADVISORY COMMITTEE

Chair, Dr. Susan M. DeBari

Dr. Paul J. Wallace

Dr. Thomas W. Sisson

Dr. Elizabeth R. Schermer

MASTER'S THESIS

In presenting this thesis in partial fulfillment of the requirements for a master's degree at Western Washington University, I grant to Western Washington University the non-exclusive royalty-free right to archive, reproduce, distribute, and display the thesis in any and all forms, including electronic format, via any digital library mechanisms maintained by WWU.

I represent and warrant this is my original work, and does not infringe or violate any rights of others. I warrant that I have obtained written permissions from the owner of any third party copyrighted material included in these files.

I acknowledge that I retain ownership rights to the copyright of this work, including but not limited to the right to use all or part of this work in future works, such as articles or books.

Library users are granted permission for individual, research and non-commercial reproduction of this work for educational purposes only. Any further digital posting of this document requires specific permission from the author.

Any copying or publication of this thesis for commercial purposes, or for financial gain, is not allowed without my written permission.

Steven D. Shaw
July 2011

H_2O CONTENTS IN OLIVINE-HOSTED MELT INCLUSIONS FROM PRIMITIVE MAGMAS IN THE NORTHERN CASCADE ARC

A Thesis
Presented to
The Faculty of
Western Washington University

In Partial Fulfillment
Of the Requirements for the Degree
Master of Science

by
Steven D. Shaw
July 2011

Abstract

The subducting Juan de Fuca plate is the hot endmember of slabs worldwide, and its unique thermal character prompts debate about the role of fluid-flux melting versus decompression melting in the Cascade arc. While slow subduction of this hot slab is expected to result in strong dehydration prior to reaching sub-arc depths, there is no consensus on whether the slab is entirely dehydrated at this point, or whether volcanism is the result of water-poor, decompression melting, or fluid-flux melting. I provide the first measurements of pre-eruptive volatile contents in olivine-hosted melt inclusions from primitive magmas in the northern region of the arc, at Mount Baker and Glacier Peak. These volatile contents and melt inclusion compositions are used to model mantle melting processes.

Low-K olivine tholeiite (LKT) and calc-alkaline basalt (CAB) melt inclusions at Glacier Peak have minimum H_2O concentrations of 2.0 and 2.2 wt. % and fO2 of ΔQFM +1.1 and +1.5, respectively. The evolved compositions of these melt inclusions in both lava types (host olivine: $Fo_{85\text{-}89}$) are corrected to mantle values by addition of ≤15 wt. % olivine, and the results suggest that the minimum water contents in the parental magmas are 1.7 wt. % and 2.0 wt. %. Measured values themselves may be low due to degassing at crustal depths. The Mount Baker Schreiber's Meadow cinder cone (CAB) has minimum H_2O concentrations of 2.3 wt. %, though these contents cannot be adequately disentangled from potential crustal involvement and/or magma mixing/mingling to be corrected to mantle values.

Results of modeling indicate that both LKT and CAB magmas at Glacier Peak are the result of 13-15% fluid-fluxed melting of a compositionally heterogeneous mantle source, last equilibrated near the base of the crust. Source regions are interpreted to contain both an ocean island basalt (OIB)-like component and a mid-ocean ridge basalt (MORB)-like component. Minimum H_2O contents suggested in the source region are between 0.21 and 0.28 wt %. This is in contrast to southern regions of the Cascade arc, where LKT magmas are considered to be the result of dry decompression melting of a MORB-like source.

Acknowledgements

This project has been made possible through funding from the following organizations: the Geological Society of America (through the Grant for Student Research), the Mazamas Foundation (Grant for Student Research), the USGS Cascades Volcano Observatory (Jack Kleinman Grant for Volcano Research), Western Washington University Graduate School (RSP Fund for the Enhancement of Graduate Research) and the Western Washington University Department of Geology (Advance for Fieldwork).

I would like to thank my advisor, Dr. Susan DeBari for encouraging me to take on this project, for her continued support and her careful (and relentless) editing. Thanks go to my committee members, Dr. Paul Wallace, Dr. Tom Sisson and Dr. Liz Schermer, for their thoughtful criticism and advice throughout the process.

I would also like to thank Dr. John Donovan, at the University of Oregon, for his help with the EPMA; Dr. Mike Rowe, at Washington State University, for his advice and his guidance while collecting and processing sulfur speciation measurements; Alison Koleszar, at Oregon State University, for her help with LA-ICP-MS measurements. I would like to thank Dr. Dan Ruscitto, at Rensselaer Polytechnic Institute, for his constant help and willingness to explain the more mundane aspects of melt inclusion work. I would like to thank Stephanie Weaver, at the University of Oregon, for her support, advice, and for letting me stay at her house. I would like to thank George Mustoe for helping me with the microscopes, for finding me random pieces of equipment and for his careful explanations and help whenever I needed it.

I would like to thank my fellow graduate students for their advice and support on all aspects of being a graduate student at WWU, from picking a clear-cut project, to keeping momentum, and mostly, "keeping the main thing the main thing." I would especially like to thank Nikki Moore for her advice and her willingness to answer a multitude of random thesis-related questions.

Finally, I would like to thank my laboratory assistant (and soon-to-be wife) Sarah Casey and my family, for their support, encouragement and confidence in me when I decided to abandon a perfectly good career to go back to school in an entirely new field.

Table of Contents

Abstract iv

Acknowledgements v

List of Tables viii

List of Figures ix

Introduction 1

Geologic Setting 6

Sampling and Analytical Methods 10

Fourier Transform Infrared Spectroscopy 10

Electron Microprobe 11

LA-ICP-MS 12

Melt Inclusions and Data Treatment 13

Results 15

Measured values, melt inclusions and olivine 15

Volatile concentrations 19

Discussion 21

Volatiles 21

Volatile Variability at Glacier Peak 22

Whitechuck 23

Indian Pass 24

Volatile Variability at Mount Baker 24

Parental Magmas 25

Temperature and Pressure 26

Melting Processes 28

Conclusions 35

Works Cited 36

Appendix A: Uncorrected Compositions 50

Appendix B: Extended Methods 52

Appendix C: Partition Coefficients.....56

List of Tables

Table 1: Corrected Compositions 43

Table 2: Olivine Compositions 47

Table 3: Mantle Compositions.....48

List of Figures

Figure 1. Map of the Cascade volcanic arc and study area 57

Figure 2. Grove model of magma generation 58

Figure 3. Melt inclusion petrography 59

Figure 4. Corrections for iron-loss.....60

Figure 5. K_2O versus SiO_2 variation diagram 61

Figure 6. Glacier Peak major element variation diagrams 62

Figure 7. Mount Baker major element variation diagrams 63

Figure 8. Glacier Peak trace element variation diagrams 64

Figure 9. Mount Baker trace element variation diagrams 65

Figure 10. Chondrite normalized rare earth element variation diagrams 66

Figure 11. NMORB normalized trace element variation diagrams 67

Figure 12. Comparison of LKT H_2O proxies.....68

Figure 13. H_2O/CO_2 variation and inclusion entrapment pressures 69

Figure 14. Variation of H_2O with alkalis and MgO 70

Figure 15. Variation of volatiles with proxies for fractionation 71

Figure 16. Temperature and pressure of entrapment and last equilibration of melt.....72

Figure 17. Nb versus Y comparison of Indian Pass and Whitechuck 73

Figure 18. EMORB normalized trace element diagram of Indian Pass 74

Figure 19. Potential decompression melt source compositions.....75

Figure 20. H_2O-K_2O-Na_2O ternary diagram 76

Introduction

Fluid-flux melting is commonly accepted as the primary driver of arc magmatism worldwide (Anderson, 1974; Fyfe and McBirney, 1975; McBirney, 1969; Sisson and Grove, 1993); however, decompression melting does play a part in some arc magmatism (Cervantes and Wallace, 2003; Grove et al., 2002; Johnson et al., 2009; Sisson and Bronto, 1998; Sisson and Layne, 1993). The Cascade volcanic arc (Figure 1) has been described as a "hot" endmember arc worldwide in terms of subducting plate temperature (Green and Harry, 1999; Leeman et al., 2005a) and its unique thermal structure has prompted debate about the relative roles of fluid-flux (wet) melting versus decompression (dry) melting in magma generation. Resolving this question has centered on characterization of volatile contents and trace element geochemistry of primitive, mafic magmas, which frequently occur in monogenetic cinder cones throughout the arc.

The Cascade arc displays diversity in the geochemical composition of these most primitive magmas. Three major compositional types have been described: calc-alkaline basalts and basaltic-andesites (CAB), low potassium olivine tholeiites (LKT), and ocean island basalt (OIB)-like basalts (Bacon, 1997; Borg et al., 1997; Conrey et al., 1997; Green and Harry, 1999; Leeman et al., 2005a; Reiners, 2000). These compositional types have been attributed to generation by distinct sources and processes (e.g. Bacon, 1997; Leeman et al., 2005a; Leeman et al., 1990).

Thorough characterization and interpretation of the origin of Cascade arc LKTs and CABs has been an ongoing process (Bacon, 1997; Borg et al., 1997; Conrey et al., 1997; Green and Harry, 1999; Green and Sinha, 2005; Grove et al., 2002; Le Voyer et al.,

2010; Leeman et al., 2005a; Leeman et al., 1990; Leeman et al., 2005b; Moore and DeBari, submitted; Reiners et al., 2000; Rowe et al., 2009; Ruscitto et al., 2010b; Schmidt et al., 2008; Sisson and Layne, 1993; Streck et al., 2007). LKTs have low potassium (≤0.6 wt. % K_2O), high aluminum (≥16 wt. % Al_2O_3) and are distinct; their geochemical signatures resemble those of mid-ocean ridge basalts (MORB) (Bacon, 1997; Leeman et al., 2005a). Like MORB, they have low abundances of incompatible elements; however they often have a small enrichment in large-ion lithophile elements (LILE) such as Ba, Sr and Pb (Bacon, 1997; Leeman et al., 2005a; Schmidt et al., 2008). The CAB and basaltic andesites have variable enrichments of LILEs, which is commonly known as an arc signature (Bacon, 1997; Leeman et al., 2005a). The LKTs have been proposed to be a result of decompression (dry) melting, while the origin of the CABs is less clear.

A model by Grove et al. (2002) explains generation of distinct CAB and LKT compositions at Mt. Shasta, in the southern Cascade arc, as melts of variably fluxed sub-arc mantle. To discern source characteristics, they use water content estimates, trace element and isotopic abundances, and experimental pressure and temperature constraints. They propose that while mantle convection results in shallow decompression melting (represented by LKTs); calc-alkaline basalts are caused by fluid-flux melting. Mantle material carried up with convection currents towards the wedge corner would melt due to decompression, depleting the mantle. This depleted source would descend along the slab/wedge interface, gaining fluids released from the subducting slab, which would cause fluid-flux melting (represented by the CABs) (Figure 2) (Grove et al., 2002). In

this model, H_2O contents of calc-alkaline primitive magmas are expected to overlap with typical arc H_2O concentrations, between 1-6 wt. % (Wallace, 2005), whereas low potassium tholeiites are expected to have low H_2O, less than 1 wt. % (Sisson and Bronto, 1998; Sisson and Layne, 1993; Wallace, 2005).

In contrast to the Grove et al. model, Leeman et al. (2005a) propose that both LKT and CAB in the southern Washington Cascades are produced by melting at different depths and temperatures in a vertical profile beneath the arc. Decompression melting of the mantle wedge produces LKT lavas. CAB lavas are then formed when rising decompression melts heat mantle components that retain a trace element arc-signature (enrichment of LILE trace elements that fractionate in fluid phases) from previous episodes of arc magmatism (Leeman et al., 2005a). These "fossilized" slab components can explain the slight LILE enrichments seen in LKTs within the Cascade arc and LILE enrichments seen far east of the arc axis (Hart et al., 1984). Further, they predict that, because the subducting slab becomes younger in the northern portion of the Cascade arc (due to oblique subduction—Figure 1) any fluid-flux component would become negligible; as the slab becomes hotter, slab dehydration would occur closer to the plate margin, eliminating the fluid component (Leeman et al., 2005a). While Mt. Shasta CAB lavas have been shown to have a fluid-flux component (Le Voyer et al., 2010; Ruscitto et al., 2010a; Sisson and Layne, 1993), Leeman et al. (2005a) suggest that this may be an anomalous feature of that region that is unrepeated elsewhere.

The best test of the relative roles of fluid-flux and decompression melting is to directly measure pre-eruptive volatile contents in primitive magmas. In the southern

Cascades (at Mount Shasta and Medicine Lake), melt inclusion studies support the low (<1 wt% H_2O) nearly anhydrous nature of LKT magmas, and the wet (up to 5 wt % H_2O) nature of the CAB magmas (Anderson, 1974; Le Voyer et al., 2010; Sisson and Layne, 1993). In the central arc, recent work by Ruscitto et al. (2010b) has shown that CAB in the Oregon Cascades have initial water contents that overlap with arcs worldwide (1.7 to 3.6 wt.%). Their interpretation is that these water contents (and their correlation to proxies for water) indicate a small amount of slab-derived fluid that is added to the mantle wedge.

Volatile characterization has yet to be extended to the northernmost segment of the Cascade arc, the Garibaldi volcanic belt (GVB) (Figure 1). No direct measurements of volatile contents in primitive magmas in the GVB have been made. Relatively primitive mafic magmas are rare, but do exist in this segment, and share the compositional diversity of primitive magmas shown in southern regions (Moore and DeBari, submitted; DeBari et al., submitted).

Characterization of primitive melt volatile contents is commonly undertaken through analyses of melt inclusions in early-formed minerals such as olivine in basaltic tephra. As olivine crystals grow, they entrap small parcels of melt. These melt inclusions are preserved as glass within their host crystals, and volatiles are dissolved within that glass. The advantage of analyzing melt inclusions is that they represent the most primitive melt composition that can be sampled directly. Once trapped, they are not affected by further magmatic processes common in the crust, such as fractionation of

multiple minerals, assimilation or mixing (Danyushevsky et al., 2002; Kent, 2008; Sobolev and Chaussidon, 1996).

In this paper, I present measured magmatic volatile concentrations from Mt. Baker and Glacier Peak in the GVB and add to the growing dataset of primitive magma compositions along the Cascades arc. These data are crucial to assessing melt generation models as they pertain to the northern arc.

Geologic Setting

The Cascade volcanic arc results from subduction of the Juan de Fuca, Explorer, and Gorda lithospheric plates beneath the western edge of North America (Figure 1). The arc is approximately 1200 km in length and was initially split into five segments based on volcanic center density and output (Guffanti and Weaver, 1988). More recently, Schmidt et al. (2008) redefined the segments based on isotopic variability, splitting the arc into four segments, and redefining the southern Washington Cascade segment based on its geochemically distinct basement rock, the Siletz terrane.

In the southern and central segments, where volcanic output is relatively high, volcanic vents are densely spaced and eruptive activity extends both into the forearc and backarc regions. This has been interpreted as the result of regional extension (Hughes and Taylor, 1986). In the northern segment, the Garibaldi Volcanic Belt (GVB), volcanic output is low, vents are sparsely separated, and there is no eruptive activity noted in the forearc and backarc regions. The GVB is ~330 km long, beginning just south of Glacier Peak and ending at Mt. Meager in British Columbia. The crust in this region is composed of metamorphosed oceanic terranes (Brown, 1987) between 40-45 km thick and the depth to the slab/wedge interface is generally considered to be between 80-100 km (McCrory et al., 2004; Mooney and Weaver, 1989; Parsons et al., 1998). The age of the slab beneath Glacier Peak and Mount Baker is estimated at < 22 Ma (Green and Harry, 1999; Wilson, 1988).

Glacier Peak, the southernmost GVB volcanic center, is a dacitic stratovolcano that has been active for the past 700 ka (Tabor and Crowder, 1969). Low-K olivine

tholeiite (potential “decompression type”) and calc-alkaline basalt (potential “fluid-flux type”) tephras have erupted near Glacier Peak at the Whitechuck and Indian Pass cinder cones, respectively (DeBari et al., submitted). Taylor (2001) described the petrography and geochemistry of four mafic lavas in the Glacier Peak area, including the Indian Pass (CAB) and Whitechuck (LKT) cinder cones used in this study. Whitechuck tephra are generally aphyric, with ≤5% phenocrystic assemblage dominated by olivine with minor plagioclase. Clinopyroxene does not occur as phenocrysts, but is found in the groundmass. Indian Pass tephras have a slightly higher percentage of phenocrysts (≤10%), again dominated by olivine (~7%), with minor plagioclase and no clinopyroxene, other than in the groundmass (Taylor, 2001). Whereas Indian Pass lavas meet the major and trace element standards for a primitive magma established by the Basaltic Volcanism Study Project (1981) (MgO > 6 wt. % and Mg# >55; Ni>100 ppm and Cr >200 ppm), Whitechuck LKT lavas have MgO > 6 wt.% , low Ni (between 55-75 ppm) and low Cr (150-175 ppm) indicative of fractionation of olivine and probably chromite.

Based on whole rock analyses and mineral chemistry, Taylor (2001) establishes that these mafic cones are likely derived from two distinct mantle sources, a depleted mantle, similar to mid-ocean ridge basaltic sources (MORB), for the Whitechuck LKT, and a more enriched source for the CABs (including Indian Pass). All lavas have the characteristic high LILE/HFSE indicative of a subduction input (either fossilized or contemporaneous). Whitechuck LKTs are interpreted as the result of high degrees of anhydrous melting of a depleted source. High LILE/HFSE ratios are explained as the sign

of a fossilized subduction component. The Indian Pass CABs are interpreted to result from lower degrees of fluid-fluxed melting of a less depleted source.

Mount Baker, the northern neighbor of Glacier Peak by ~90 km, is an andesitic stratovolcano. Calc-alkaline basalt (potential "fluid flux type") tephras and flows are present to the south of Mount Baker, at the monogenetic Schreiber's Meadow cinder cone and at the Sulphur Creek and Lake Shannon lava flows. An LKT-like composition (potential "decompression melt type") is found in the Park Butte flow (Moore and DeBari, submitted).

Moore and DeBari (submitted) distinguish three distinct primitive end-member magma types present at Mount Baker, an LKT-like basalt, a CAB endmember, and a high-Mg basaltic-andesite. One of the lava flow units, the CAB Sulphur Creek flow, is associated with the Schreiber's Meadow cinder cone used in this study. The Sulphur Creek lava flow is porphyritic, and contains ≤25% modal phenocrysts, mostly plagioclase (≤20%), with some olivine (≤5%) and minor (≤1%) clinopyroxene (Moore and DeBari, submitted). All mafic lavas studied have significant textural evidence for disequilibrium, as well as chemical disequilibrium between whole rock and mineral phases, suggesting an unidentified crustal modification of the magma or magma mixing. However, the lack of incompatible element variation and primitive isotopic signatures suggest minimal addition of crustal material. Thus Moore and DeBari (submitted) conclude that the incompatible trace element variations in these lavas are useful for characterizing mantle sources. All lavas include the high LILE/HFSE ratios typical of arcs, and LKT-like lavas have some of the highest LILE/HFSE ratios, which is unlike other Cascade LKTs.

Through melt modeling, Moore and DeBari (submitted) establish that the three end-member types are the result of two distinct mantle sources and variable melt degree, degree of differentiation and/or enrichment in slab contribution. The LKT-like basalt is interpreted to derive from a depleted spinel lherzolite source and displays the strongest enrichment in slab-derived fluids. The CAB flows (including Sulphur Creek) are interpreted to derive from a less-depleted spinel lherzolite source with the smallest enrichment in slab-derived fluids. The high-Mg basaltic-andesite end-member is interpreted to originate from a depleted garnet lherzolite source that has an intermediate enrichment in slab-derived fluids.

Sampling and Analytical Methods

Detailed sampling and analytical methods are presented in Appendix A. A summary of these methods is provided below.

Tephra samples for this study were collected from three monogenetic cinder cones—two from Glacier Peak (a primitive calc-alkaline basalt [CAB] and a primitive low-potassium olivine tholeiite [LKT]) and one from Mount Baker, a primitive CAB). LKT lavas are present at Mt. Baker, but none have associated tephra and were not sampled for this study. Olivine crystals from tephras in this study were hand-picked, temporarily mounted individually on round glass slides, and doubly polished to expose melt inclusions on two parallel sides of the host olivine. Melt inclusions were glassy, between 50 and 150 microns in diameter, generally round or oval-shaped and contained vapor bubbles (Figure 3). After polishing, host olivine crystals were removed from the glass slide for analysis.

Fourier Transform Infrared Spectroscopy

Analysis of H_2O and CO_2 in the melt inclusions was performed with a Thermo-Nicolet Nexus 670 FTIR spectrometer at the University of Oregon. Each unmounted olivine crystal was individually placed upon a NaCl wafer. Spectral analyses were repeated between three and four times, each analysis encompassing 256 individual scans. Aperture size ranged from 50—120 μm depending on inclusion diameter. Inclusion thickness, initially determined with a digital micrometer measurement of the olivine wafer, was corroborated through the use of reflectance fringes. To accomplish this, a secondary scan using reflected light was performed with each crystal, and thickness

calculated with the wavelength of reflectance fringes, as per Wysoczanski and Tani (2006). Thickness measurements typically agreed to within 5% and calculated measurements were used in almost all cases. In cases in which the fringes were indistinct the initial micrometer measurement was used. H_2O and CO_2 concentrations were calculated using the Beer-Lambert law (Dixon and Pan, 1995). Because the CO_2 absorption coefficient is dependent on the glass composition, final CO_2 concentrations were not calculated until after microprobe analysis. Determination of peak heights for CO_2 required subtraction of background noise (unpublished program, S. Newman). Initial H_2O and CO_2 concentrations, uncorrected for post-entrapment olivine crystallization (explained below), are reported in Appendix A. Due to uncertainties both in inclusion thickness and in absorbance peak heights, average uncertainty at 1 σ in H_2O and CO_2 concentrations is 11%. Accuracy of the FTIR technique is expected to be ±10% for H_2O and ±20% for CO_2 (Dixon, 1991).

Electron Microprobe

After FTIR analysis, olivine hosts were washed, mounted in epoxy and the associated melt inclusions were analyzed for major element composition with the Cameca SX100 electron probe at the University of Oregon. Beam conditions were as follows: 15 kV accelerating voltage, 20 nA beam current, and a beam diameter of 10 microns. Element count times were as follows: 10 s (Mn), 20 s (Ca, S, Cl, Ti), 30 s (Mg, Si), 40 s (K, Al, P), 60 s (Fe). Olivine host compositions were also analyzed, at a spot located a distance of ~100 microns from both the edge of the host crystal and the inclusion. Intensities were corrected by either linear off-peak background correction (K,

Mn, S, Cl, Ti and P) or the mean atomic number (MAN) background correction procedure (Na, Si, Al, Mg, Fe and Ca) of Donovan and Tingle (1996). Measured standard concentrations were within 0.07% of published values, except S, which was within 0.92 % of published values. Percent standard deviation, based on replicate analyses of each inclusion, was ≤ 5% for all elements except Mn, which was ≤7%.

The oxidation states of the magmas were determined through sulfur speciation (S^{6+}/S_{total}), which was obtained from S Kα peak shifts relative to the peak shift of anhydrite. Sulfur peak shifts were measured with the JEOL 8500F field emission electron microprobe at Washington State University (as per Carroll and Rutherford, 1988; Wallace and Carmichael, 1994). Beam conditions were as follows: 15kV accelerating voltage, 30 nA beam current, and a beam diameter of 5 microns. Count times were 5 s for standards and 30 s for unknowns. To avoid oxidation of sulfur during analysis, the beam position was moved 1 μm each 60 s of analysis. Troilite and pyrrhotite standards were run before and after the glass inclusions to monitor accuracy. Pyrite and anhydrite standards were analyzed at the start and end of the run in order to calculate sulfur speciation (Rowe et al., 2007). Precision, based on replicate analyses, was better than 10% at 1 σ for all samples, except sample IP_003 (± 13%).

LA-ICP-MS

Trace element compositions of melt inclusions were measured with a laser ablation inductively coupled mass spectrometer (VG PQ ExCell quadrupole ICP-MS and NewWave DUV 193 nm ArF Excimer laser) located at Oregon State University. Beam conditions were 3 Hz, beam size was 50 μm with a 45 s total dwell time. Dwell time per

element was 10 milliseconds. Glass standard GSE-1G was used for calibration and ^{43}Ca was used as an internal standard. Accuracy at 1σ was ≤5% from accepted values. Precision was ≤5% for trace elements Ti, V, Sr, Y, Zr, Ba and Ce, ≤10% for trace elements Sc, Rb, Nb, La, Pr, Nd, Pb, ≤15% for Sm, Eu, Hf, and Th, and ≤20% for Gd, Dy, Er, Yb, Ta and U.

Melt Inclusions and data treatment

Inclusions can undergo a number of possible post-entrapment compositional changes. These include post-entrapment crystallization of olivine on the host mineral, diffusive loss of Fe to the host olivine and diffusive loss or gain of H_2O to the host magma (Danyushevsky et al., 2000; Gaetani and Watson, 2000; Portnyagin et al., 2008).

As inclusions cool, there is continued crystallization of olivine on the rim of the inclusion, referred to as post-entrapment crystallization (PEC) (Sobolev, 1996). The effect on major element composition was corrected by adding in olivine (in steps of 0.1 wt. %) until equilibrium between host and inclusion was achieved (Sobolev and Chaussidon, 1996). The effect of PEC on trace element concentrations was corrected by utilizing the batch equilibration crystallization equation, using the % PEC to determine F (the amount of melt remaining) and using the partition coefficients for olivine presented in Appendix C.

Loss of iron occurs when continued inclusion-rim olivine crystallization is slow enough to achieve equilibrium with the rest of the host crystal. If each new increment of olivine re-equilibrates (through iron diffusion), the Mg# of the inclusion stays relatively

constant with the host. When olivine is added back into the original composition to correct for PEC, the inherited FeO^T will be low (Danyushevsky et al., 2000). Iron loss was corrected using the FeLoss computer program, developed by Danyushevsky et al. (2000), that requires an estimate of the correct FeO^T of the inclusion as a starting assumption. This estimate was arrived at by first tentatively correcting the inclusion compositions by adding in incremental olivine until equilibrium with the host was achieved. These compositions were compared to those of whole rock samples from the same units (Figure 4). If the FeO^T of the inclusions did not overlap with that of the whole rock (at a particular MgO wt. %), an estimate of FeO^T was made that would bring the inclusions in line with whole rock compositions (e.g. Vigouroux et al., 2008). Further olivine addition was then required to bring the inclusions into equilibrium with their hosts.

Portnyagin et al. (2008) demonstrate that diffusive exchange of water can occur over extremely short time-scales (less than 2 days). For this study, using quickly cooled inclusions (tephra) decreases the likelihood of post-entrapment diffusive loss of water. Diffusive loss of water before final ascent and eruption is still possible, however, and is addressed below.

Results

Measured values, melt inclusions and olivine

The twenty-three measured melt inclusion compositions are primarily basalt, with some basaltic-andesite, and one andesite (47.6-57.1 wt. % SiO_2). These compositions were subsequently corrected for post-entrapment crystallization of olivine on the crystal-inclusion interface, and potential loss of iron through diffusive exchange (see procedure above). Uncorrected, measured compositions are presented in Appendix A, corrected compositions are presented in Table 1. Melt inclusions generally share LKT and CAB composition characteristics with their host lavas.

Olivine crystals that host melt inclusions range in composition from Fo_{80}-Fo_{89} and are presented in Table 2. The most primitive hosts are seen at Indian Pass (Fo_{87}-Fo_{89}). Whitechuck olivine hosts range from Fo_{85}-Fo_{86}, whereas Schreiber's Meadow olivine hosts show the most variability and range from Fo_{80}-Fo_{86}.

Correcting for post-entrapment crystallization requires knowing Fe^{2+}/Mg ratios of both melt and host olivine. Host olivine can be assumed to have $Fe^{2+}/Fe^{T}=1$, thus Fe^{2+}/Mg ratios were obtained from the microprobe analyses reported in Table 2. In the melt, Fe^{2+}/Fe^{T} is constrained by oxygen fugacity. Oxygen fugacity of inclusions was determined through sulfur speciation (see sulfur speciation procedure above) using the empirically derived equation of Wallace and Carmichael (1994), relating sulfur speciation and oxygen fugacity of magmas. Oxidation states (relative to the Quartz-Fayalite-Magnetite (QFM) buffer) for the Whitechuck LKT cinder cone are ΔQFM +1.0 to +1.5 (average ΔQFM +1.3). Oxidation states for Indian Pass CAB inclusions range

from ΔQFM +1.6 to +1.8 (average ΔQFM +1.7). Oxidation states for Schreiber's Meadow CAB range from ΔQFM +1.0 to +1.3 (average ΔQFM+1.2). These fugacity values require an initial Fe^{2+}/Fe^{T} of 0.84 for Whitechuck, 0.80 for Indian Pass, and 0.83 for Schreiber's Meadow, calculated as described in Borisov and Shapkin (1990).

DeBari et al. (submitted) do not report fO_2 for Glacier Peak magmas, though they note that it is probably between QFM and the nickel-nickel oxide (NNO) buffers, which is similar, though slightly lower than these results. These oxygen fugacities add to those determined at Mount Baker by Moore and DeBari (submitted). They calculated oxygen fugacity for two of Mount Baker's endmember primitive magma types based on Fe-Ti oxides: the Park Butte LKT-like flow (ΔQFM +2.3 to +2.4; average +2.3), and the Tarn Plateau high-Mg basaltic andesite (ΔQFM +1.4 to +3.2; average +2.1). Neither of Mount Baker's calc-alkaline lava flows (the primitive Lake Shannon or more differentiated Sulphur Creek) contain an ilmenite endmember suitable for these calculations. However, as they noted, temperatures calculated from the Park Butte and Tarn Lake mineral pairs were substantially low, indicating sub-solidus re-equilibration of Fe-Ti oxides.

The olivine Fo values from Table 2, along with appropriate distribution coefficient (K_D) values for Fe/Mg equilibria in olivine-liquid pairs, were used to calculate equilibrium melt inclusion Mg#s. Kd values were determined as per Toplis (2005). Average Kd values were: 0.32 ±0 .01 (Whitechuck), 0.31 ±0.02 (Indian Pass), and 0.32 ±0.02 (Schreiber's Meadow).

Major element compositions of melt inclusions were corrected for post-entrapment crystallization of olivine. Trace element and volatile concentrations were also

corrected for post-entrapment crystallization, though due to their generally incompatible nature in olivine, these corrections were minor. Olivine was incrementally added back into the melt inclusion compositions until the inclusion compositions were in equilibrium with their host olivine. Most Whitechuck inclusions required additional olivine ≤4.7 wt. % (one inclusion required 8.2 wt. %). Indian Pass inclusions required additional olivine between 0.6 and 5.2 wt. % (average 3.5 wt. %). Schreiber's Meadow inclusions required additional olivine between 0.9 to 7.0 wt. % (average 3.6 wt. %).

Oxygen fugacity must also be corrected for post-entrapment crystallization; as Fe^{2+} is added back into the system, the Fe^{2+}/Fe^{T} ratio will change. Oxygen fugacity was corrected by calculating new fO2 as each new 0.1 wt. % increment of olivine was added back into the inclusion composition. Corrected oxidation states for the Whitechuck LKT cinder cone are ΔQFM +0.8 to +1.4 (average ΔQFM +1.1). Oxidation states for Indian Pass CAB inclusions range from ΔQFM +1.4 to +1.5 (average ΔQFM +1.5). Oxidation states for Schreiber's Meadow CAB range from ΔQFM +0.7 to +1.1 (average ΔQFM+1.0). Corrected oxidation states are presented in Table 1.

A total of eight inclusions were corrected for post-entrapment iron-loss (Figure 4). Three inclusions from Whitechuck required an average of 0.84 wt. % addition of FeO^{T}. Three inclusions from Indian Pass required an average of 0.44 wt. % addition of FeO^{T}. Two inclusions from Schreiber's Meadow required an average of 0.68 wt. % addition of FeO^{T} (Table 1).

Corrected major element compositions for melt inclusions in the calc-alkaline lavas (Schreiber's Meadow at Mt. Baker and Indian Pass at Glacier Peak) generally fall

within the medium-K calc-alkaline basalt to basaltic-andesite field (Figure 5). However, one Indian pass melt inclusion is a high-K basaltic andesite. One Schreiber's Meadow melt inclusion is a high-K andesite and one is a low-K tholeiitic basaltic andesite. Melt inclusions for the Whitechuck LKT extend from the low-K tholeiite field to the boundary between LKT and medium-K basalt (Figure 5). These compositions are consistent with whole rock analyses of these sites and also overlap with calc-alkaline and tholeiitic compositions along the Cascade arc (Figure 5).

Major elements plotted on Harker diagrams (all elements are compared on an anhydrous basis) show good overlap with the bulk rock compositions at Whitechuck (Figure 6). Indian Pass major elements are slightly offset (i.e.: higher CaO, Na_2O, TiO_2, Al_2O_5 and lower MgO, FeO^T all at lower SiO_2) from whole rock compositions, yet cluster tightly, except for sample IP_005, which is more evolved and shows evidence of significant degassing (see below). Schreiber's Meadow inclusions show the most extreme scatter in comparison with bulk rock from the associated Sulphur Creek lava flow (Figure 7).

Trace element compositions are generally more variable than major elements seen in the melt inclusions. However, Whitechuck trace element compositions are relatively homogeneous, and overlap tightly with bulk rock compositions. Indian Pass compositions are slightly offset to higher (Ba, La, Nd, Sr) or lower (Rb, Yb, and Zr) values at lower SiO_2 (Figure 8). Schreiber's Meadow inclusions are the most variable, and do not group tightly near bulk rock compositions (Figure 9).

Rare earth element patterns and trace element diagrams reflect the varying degrees of overlap or, alternatively, scatter seen in Harker diagrams. Whitechuck rare-earth element (REE) patterns overlap those of bulk rock analyses. Both Indian Pass and Schreiber's Meadow REE patterns are more variable than their respective bulk rock compositions—however average values for Indian Pass compositions overlap whole rock compositions (Figs 10, 11). Even with the variability, trace element patterns from melt inclusions corroborate data recorded by whole rocks. Glacier Peak LKT have flatter REE patterns and lower abundances of high-field strength elements (HFSE) and middle REE than CAB at Mount Baker and at Glacier Peak. Glacier Peak CAB have steeper REE than CAB at Mount Baker. LILE elements are enriched in all three units, and some LILE/HFSE ratios are higher at Whitechuck (Ba/Nb ~75, Pb/Ce~0.18) in comparison to either Schreiber's Meadow (Ba/Nb ~ 51, Pb/Ce~0.12) or Indian Pass CAB (Ba/Nb ~51, Pb/Ce~0.12). Proxies for H_2O (Ba/Zr and Pb/Ce) span the range of LKT in the southern arc (Figure 12), though Pb/Ce extends to higher values than elsewhere.

Volatile concentrations

Volatile concentrations were corrected for post-entrapment crystallization (above) and are presented in Table 1. Corrected for post-entrapment crystallization, Whitechuck melt inclusion H_2O concentrations are 0.5-2.0 wt % (average 1.3 wt %). CO_2 concentrations range from 155 ppm to as high as 821 ppm (average 485 ppm), S concentrations are 1200-1690 ppm, and Cl is 910-1010 ppm.

Corrected Indian Pass H_2O contents are 1.1-2.2 wt. % (average 1.6 wt. %), CO_2 concentrations are between <50 ppm to 1720 ppm (average of measurable CO_2, 1140 ppm), S concentrations are 2550-3320 ppm, and Cl concentrations are 418-711 ppm.

Schreiber's Meadow inclusions have corrected H_2O contents of 0.8-2.3 wt. % (average 1.6 wt. %), CO_2 concentrations of <50 ppm-870 ppm (average of measurable 451 ppm), S concentrations between 170 (in the andesitic inclusion) and 1526 ppm, and Cl concentrations of 205-477 ppm (Table 1).

H_2O and CO_2 concentrations have been used to indicate entrapment pressures based on known solubilities in basaltic magmas. Vapor saturation pressures were calculated for each inclusion using the VolatileCalc program (Newman and Lowenstern, 2002) (Table 1, Figure 13). Entrapment pressures range from 6 to 374 MPa, though these calculated pressures may be affected by H_2O or CO_2 variability due to degassing, loss of CO_2 to a shrinkage bubble post-entrapment, or post-entrapment loss of H_2O due to diffusion. Therefore these pressures should be considered minimum entrapment pressures. The potential effects of degassing on measured volatile concentrations (and therefore calculated pressures) will be further developed below. Whitechuck inclusions record entrapment conditions between 44 and 202 MPa, Indian Pass between 82 and 374 MPa and Schreiber's Meadow between 6 and 255 MPa. These conditions correspond to crustal entrapment depths ranging between 0.2 and 12 km (assuming average upper crustal density of 2.8 g/cm^3). Recorded maximum entrapment depths are: ~7 km (Whitechuck), ~12 km (Indian Pass) and ~9 km (Schreiber's Meadow).

As vapor exsolves from a rising magma, the liquidus temperature of the magma increases, resulting in crystallization. Therefore, crystallization may be expected to correlate with loss of water (e.g. Sisson and Layne, 1993). At Schreiber's Meadow, with the exception of two inclusions, H_2O loosely correlates negatively with K_2O and Na_2O and positively with MgO—expected correlations for a magma that is exsolving H_2O and crystallizing as it rises (Figure 14).

Indian Pass H_2O concentrations show a loose negative correlation with K_2O, but H_2O does not show a correlation with decreasing MgO (Figure 14). Thus, it is difficult to make any interpretation of simultaneous crystallization accompanying degassing at Indian Pass.

At Whitechuck, no trends are seen with changes in H_2O content (Figure 14). An explanation for this may be rapid syneruptive degassing, which would not result in significant crystallization, as seen at Mount St. Helens (Blundy and Cashman, 2005).

Discussion

Volatiles

The use of olivine-hosted melt inclusions in primitive magmas is intended to discern volatile concentrations in the most primitive magma in a system and relate these concentrations to mantle source compositions and processes. However, interpretations are predicated on the assumption that these volatile contents are not the result of either crustal interaction or post-entrapment changes. These assumptions may be invalidated by

pre-entrapment assimilation of crustal material or mixing with a second, volatile-rich magma. Complicating matters further, volatile content is constantly being adjusted due to degassing (volatile depletion) and pre-entrapment fractionation (incompatible volatile enrichment). There is also experimental evidence for open-system behavior of some volatiles such as H_2O (changed via hydrogen diffusion) (Portnyagin et al., 2008). I evaluate some of these complications below, in regards to measured H_2O contents at Glacier Peak and Mount Baker.

Volatile Variability at Glacier Peak

Pre-entrapment magma mixing is unlikely at Whitechuck or at Indian Pass as no chemical or petrographic evidence for this process is observed (this study; DeBari et al., submitted). Isotopic data presented by DeBari et al. (submitted) suggest that both Whitechuck and Indian Pass are internally isotopically homogeneous, in contrast to Glacier Peak's Lightning Creek basaltic andesite, which does show both chemical and petrographic evidence for extensive mixing with crustally-derived dacite. Thus, H_2O contents of Whitechuck and Indian Pass magmas are not expected to have been elevated by mixing with other, more H_2O-rich magmas.

Only minimal crystal fractionation is probable at Indian Pass given its nearly aphyric nature and high Cr and Ni contents in whole rock analyses, which are above established minimum values for a primitive composition (Ni> 100 ppm, Cr >200 ppm) (DeBari et al, submitted). Also, as noted earlier, H_2O contents show a loose anti-correlation with increasing K_2O wt. % (a proxy for fractionation) at Indian Pass. At

Whitechuck, tephras are aphyric, but low Cr and Ni contents in whole rock analyses (DeBari et al., submitted) suggest higher amounts of pre-entrapment fractionation of olivine. Corrections for this additional crystal fractionation are made below.

Due to the primitive nature of Indian Pass CAB magmas, and the low Rb and Sr of Whitechuck LKT, similar to other arc LKTs, crustal contamination is also unlikely (Taylor, 2001). Thus, measured H_2O and other volatile concentrations are assumed to be indicative of mantle melt sources, enriched through variable amounts of fractionation, and potentially affected by degassing or diffusion.

Whitechuck

H_2O concentrations (corrected for post-entrapment crystallization) for the Whitechuck LKT magma (up to 2.0 wt. %) are within typical arc values, between 1 and 6 wt. % (Wallace, 2005). H_2O and other volatile contents show wide-ranging variability, despite the homogeneity of the magma (Figure 15). While low, the measured values are still higher than expected, as the source for the Whitechuck LKT magmas has been previously interpreted as relatively anhydrous (Taylor, 2001), similar to other Cascade LKT magmas. Measured H_2O concentrations and the slightly stronger arc trace element signature seen in this northern LKT are permissive of a more prominent role for fluid-flux melting. Based on the relative primitiveness of the Whitechuck LKT and the lack of evidence for magma mixing or crustal contamination, I conclude that H_2O variability is likely due either to pre-entrapment degassing or post-entrapment diffusion through the host olivine or some combination of both. Thus, maximum measured H_2O contents at Whitechuck are taken as minimum values and are used when correcting for the effect of

fractionation from mantle sources. These H_2O contents are also in good agreement with estimated H_2O contents (max ~2 wt. %) determined utilizing measured major element compositions of plagioclase phenocryst rims (collected by Taylor, 2001), the Ca/Na ratio of the melt (represented by the whole rock compositions), and the Ca/Na plagioclase hygrometer of Lange et al. (2009).

Indian Pass

H_2O concentrations (corrected for post-entrapment crystallization) at Indian Pass (up to 2.2 wt. %) also overlap the low end of arcs (Table 1). While no evidence for crustal interaction processes is evident (as discussed above; DeBari et al., submitted), degassing and diffusion may have affected H_2O concentrations. However, measured H_2O contents are in good agreement with those determined by the hygrometer (max ~2 wt. %) of Lange et al. (2009). Again, I will assume that maximum measured values are representative of minimum values in the primitive magma.

Volatile Variability at Mount Baker

At the Sulphur Creek lava flow, associated with the Schreiber's Meadow cinder cone, there is significant petrographic and chemical evidence for disequilibrium, indicative of magma mixing (Moore and DeBari, submitted). It is therefore likely that H_2O content at Schreiber's Meadow have been affected by crustal interaction. There are much more primitive calc-alkaline basalts present at Mount Baker (i.e. Lake Shannon), yet these have no associated tephra (Hildreth et al., 2003) and are therefore not utilized in this study.

H_2O contents at Schreiber's Meadow also overlap at the low end of arcs (up to 2.3 wt. %), and agree with the plagioclase hygrometer (max ~2 wt. %) of Lange et al. (2009). Decreasing H_2O with increasing alkalis, as well as a positive correlation with MgO (Figures 14,15), are consistent with degassing associated with crystallization and thus the maximum concentrations may be taken as minimum values within the crust. However, due to the significant evidence for disequilibrium (petrographic textures, variability of both major and trace elements), I do not refer to Schreiber's Meadow in the following discussions about mantle source compositions or associated H_2O contents in the southern Garibaldi volcanic belt.

Parental Magmas

While olivine-hosted melt inclusions record the most primitive magma accessible for analysis, they typically do not record compositions in equilibrium with their initial mantle source peridotite (olivine Fo≥90). Therefore, further corrections must be made in order to estimate the compositions of the parental melts of these primitive magmas. The simplest assumption is that the primitive magmas (as represented by the melt inclusions) have fractionated primarily olivine since last equilibration with the mantle. While the whole rock phenocryst assemblage contains minor (<1 %) plagioclase, this method of olivine addition is supported by isobaric, equilibrium crystallization modeling of the measured primitive melts by entering calculated parental melts into both the PETROLOG program (Danyushevsky and Plechov, 2008) and into the MELTS algorithm via the Adiabat interface (Smith and Asimow, 2005). This modeling indicates that olivine is the

major crystallizing phase until 11% crystallization (both PETROLOG and MELTS) for Indian Pass compositions and until either 16% crystallization (PETROLOG) or 14% crystallization (MELTS) for Whitechuck compositions. After these amounts of crystallization are achieved, plagioclase becomes a fractionating phase, explaining its minor presence in the final phenocryst assemblage. Assuming mantle wedge olivine to be Fo_{90}, corrections for crystal fractionation (using the same method and partition coefficients as for post-entrapment crystallization) were made to equilibrate inclusion compositions to mantle compositions. Addition of 13.6-15% olivine was necessary to bring Whitechuck melt inclusion compositions to equilibrium with mantle olivine, and 5.5-7.7 wt. % olivine addition was required for Indian Pass. These calculated equilibrium mantle melt compositions (trace elements, major elements and volatiles) are presented in Table 3.

Temperature and Pressure

The ultimate aim of this study is to constrain melt generation processes in the northern Cascade arc. To do this, calculated equilibrium mantle melt compositions (and associated minimum H_2O contents) from Glacier Peak are used to constrain temperature and pressure conditions of the primary melt as it segregated from the mantle and to model source composition[s], potential slab inputs and their compositions.

Using the melt geothermometer and barometer of Lee et al. (2009) with calculated equilibrium mantle melt compositions, conditions of last equilibration with the mantle would have been 1278-1317 (±40)°C and 1.2-1.6 (±0.2) GPa for Whitechuck and

between 1237-1250 (±40)°C and 0.9-1.4 (±0.2) GPa for Indian Pass (Figure 16). The lowest calculated equilibration pressure at Indian Pass is obtained from sample IP_005, which has an anomalous composition (Figs. 6, 8), and is unlikely to be representative—other pressures range between 1.2 and 1.4 GPa.

Calculated pressures place equilibration at depths of 41-54 (±7) km (mafic crustal density of 3.0 g/cm^3) for Whitechuck and between 45-48 (±7) km for Indian Pass. Crustal depth is considered to be between 40 and 45 km (Mooney and Weaver, 1989), therefore, the minimum depth of equilibration should be considered to be at or near the base of the crust (Figure 16). This would place depths within the spinel peridotite field. This is consistent with REE patterns, which are not highly depleted in HREE and enriched in LREE, as are those expected with magmas equilibrated within the garnet stability field. Surprisingly, within error, Whitechuck and Indian Pass magmas equilibrated at the same, or a quite similar depth. Calculated temperatures of Indian Pass CAB are 8-45°C cooler than the mantle dry solidus temperature of Hirschmann (2000) (33-45°C cooler when IP_005 is excluded) and Whitechuck equilibration temperatures are between 4°C cooler to 6°C hotter than the dry solidus. An adjustment of -35°C to the dry solidus calculation of Hirschmann (2000) is recommended by Katz et al. (2003), placing Indian Pass compositions at or near the solidus and Whitechuck compositions ~40°C hotter than the solidus. In either case, within error of the geothermometer and geobarometer (±0.2 GPA and ±40°C), melts could have equilibrated at temperatures below the solidus (indicative of fluid-fluxed melting) or above the solidus (permissive of dry decompression melting).

Melting Processes

Measured H_2O values and calculated mantle equilibration temperatures all are permissive of fluid-fluxed melting. I evaluate the following potential mantle sources and melting scenarios to constrain whether they can produce the observed H_2O contents in Glacier Peak LKT and CAB magmas. These include 1) dry decompression melting of a source with no hydrous phases (limited hydration capacity in anhydrous minerals), 2) dehydration melting of a metasomatized mantle source with hydrous phases, or 3) fluid-fluxed melting of a mantle source. In each case, the maximum measured H_2O contents (assumed to be the minimum content in the primitive magma), further corrected to mantle equilibration (Fo_{90}), are used [1.7 wt % for LKT, 2.0 wt. % for CAB (Table 3)]. To be permissible, melt processes must be compatible with measured H_2O concentrations, calculated primary melt compositions, and likely mantle source characteristics.

Mantle source characteristics can be identified by focusing on trace elements that are not considered to be enriched from a slab component (such as Nb, Zr, Y, Yb and Ti), known collectively as conservative elements. Plots of these elements, such as Nb and Y (Figure 17), indicate two distinct mantle sources for the LKT and CAB magmas; one more depleted (Whitechuck LKT) and one more enriched (Indian Pass CAB). For the Whitechuck LKT, the possible depleted mantle source is likely compositionally similar to a MORB source (Figure 17). This is further supported by spinel Cr#/olivine Fo systematics reported by Taylor (2001). Nb/Y systematics suggest that the enriched mantle source for the Indian Pass CAB may be similar to that of an enriched mid-ocean ridge basalt (EMORB) (Figure 17). Corrected Indian Pass trace elements were normalized to

EMORB and plotted against an EMORB composition (which plots as a straight line at 1). Conservative elements from Indian Pass plot at or near 1 (excepting Zr), lending further support for an EMORB-like source (Figure 18). These source compositions (a depleted mantle source for Whitechuck LKT and an enriched mantle source for Indian Pass CAB) place an additional constraint on magma generation processes.

If dry decompression melting is responsible for magma genesis, then the H_2O contents of the Glacier Peak LKT and CAB could be the result of varied amounts of partial melting of a nominally anhydrous mantle wedge. The storage capacity of H_2O in the mantle is between 300 and 1000 ppm (Dixon, 2001; Dixon et al., 2002; Jamtveit et al., 2001). Assuming the maximum H_2O storage capacity of the mantle, solving for the simple batch melting equation shows that the maximum partial melt of a mantle source containing ~1000 ppm H_2O, would be ~3.8% melt (Whitechuck) or ~3.5 wt. % melt (Indian Pass), assuming a mantle/melt partition coefficient for H_2O of 0.012 (Stolper and Newman, 1994; Workman and Hart, 2005). Then, solving the batch melting equation for each individual trace element utilizing these melt fractions (partition coefficients for incompatible trace elements in peridotite are also from Workman and Hart, 2005), the trace element signature of the mantle source peridotite can be determined for a dry melting scenario (with no hydrous phases). While this modeling does suggest two separate source regions (Figure 19), both are more depleted in conservative elements (Nb, Zr, Y, Yb, Ti) than the mantle source constraints determined above. Thus, dry decompression melting of a source with no hydrous phases is not a permissible melt generation scenario.

Alternatively, H_2O could potentially be stored in hydrous mantle phases. Decompression-driven partial melting of these hydrous phases could account for high amounts of H_2O, including (and in excess of) measured concentrations, independent of fluid-fluxed melting. Such phases might include antigorite, amphibole, talc, chlorite or phlogopite. However, of these phases, only phlogopite is stable at pressures and temperatures expected within the mantle wedge beneath the arc (Fumagalli and Poli, 2005; Grove et al., 2006; Poli and Schmidt, 2002; Yoder Jr and Kushiro, 1969). Amphibole, for example, is only stable to ~1100 °C, limiting its presence to just above the subducting slab (Holloway and Burnham, 1972). Stoichiometrically, phlogopite contains K_2O and H_2O in a ratio of 2:1. Relationships between source region phases and abundances of H_2O, K_2O and Na_2O were explored on a ternary diagram for four arc volcanoes (Sisson and Layne, 1993), who determined that melting of phlogopite would shift compositions heavily towards K_2O (Figure 20). One would expect, then, that the K_2O/H_2O ratio at either Indian Pass (K_2O/H_2O: average 0.53, excluding degassed inclusion 0.65), or at Whitechuck (K_2O/H_2O average 0.28, or, excluding the three most degassed inclusions, average 0.73) would be much higher if derived from a source containing phlogopite. Thus, dry melting of a mantle source containing hydrous phases is incompatible with calculated primary melt compositions.

While both decompression melting scenarios can account for measured H_2O concentrations, they are either incompatible with mantle source compositions or with calculated primary melt compositions. Therefore, fluid-fluxed melting may account for generation of both LKT and CAB magmas. This is inconsistent with the complete

dehydration of the downgoing slab predicted in hot arcs (e.g. Leeman et al., 2005b) and supported by some thermal models of arcs (Hacker, 2008). However, newer thermal models suggest that while the sediment and crustal components of the subducting slab are entirely dehydrated, the slab can contain H_2O in serpentinized slab mantle, if only to depths of 115 km (van Keken et al., 2011).

To evaluate the possibility that fluid-fluxed melting can account for both LKT and CAB magmas at Glacier Peak; I model fluid-fluxed melting of a heterogeneous mantle wedge, starting with the constraints on mantle sources (depleted source for Whitechuck LKT and an enriched source for Indian Pass CAB) and following the method of Portnyagin et al. (2007). As mantle wedge source material has likely undergone some previous melt extraction (PME), Portnyagin et al. (2007) developed a method to calculate how much (if any) PME is required of a typical source composition (e.g., MORB or EMORB source) to most closely match the actual source that would be melted to create a calculated parental melt. Using this source composition, the degree of melting (F) of a mantle source (corrected for PME) can then be determined (e.g. Kelley et al., 2006; Kelley et al., 2010; Portnyagin et al., 2007). In addition to the amount of melting and PME, the procedure of Portnyagin et al. (2007) creates an estimate of the composition of the fluxed slab contribution.

The initial mantle source compositions are similar to MORB (Whitechuck LKT) and EMORB (Indian Pass CAB). Two depleted MORB sources are reported in the literature (Salters and Stracke, 2004; Workman and Hart, 2005), and both were evaluated as potential (pre-PME) Whitechuck LKT mantle sources. A commonly used EMORB

source (for Indian Pass CAB) is not reported in the literature. However, a similarly heterogeneous mantle is noted in the Trans-Mexican Volcanic Belt, where enriched EMORB-like source regions are interpreted to result from previous melt extraction of an enriched OIB-like source followed by addition of a slab component (Vigouroux et al., 2008). Other workers have also considered CAB arc magmas to be the result of variably depleted OIB-like mantle sources contaminated with a subduction component (Johnson et al., 2009; Ruscitto et al., 2010b). To constrain CAB petrogenesis in the Central Oregon Cascade arc, Ruscitto et al. (2010b) assumed that three different central Cascade OIB compositions (Rowe et al., 2009) were each the result of 5% melting of variably enriched mantle sources. Using these three OIB compositions, they reconstructed initial mantle source compositions. Though there are no known eruptions of OIB-like magmas at Mount Baker or at Glacier Peak, an OIB-like component in the mantle wedge is interpreted throughout the Cascade arc (Conrey et al., 1997; Leeman et al., 1990; Rowe et al., 2009; Schmidt et al., 2008). Since an OIB-like component is a common Cascade arc feature, three Cascade arc OIB-sources from Ruscitto et al. (2010b) were evaluated as potential (pre-PME) Indian Pass CAB mantle sources.

The best fit for the average calculated Whitechuck parental melt indicates a mantle source similar to either the DMM of Salters and Stracke (2004), with previous melt extraction of 0.001 mass fraction, or a mantle source that is similar to the E-DMM of Workman and Hart (2005), with PME of 0.002 mass fraction. The best fit for the average Indian Pass parental melt indicates a source similar to that of the Central Oregon Cascade OIB sample WFO21 (Ruscitto et al., 2010b), with no previous melt extraction.

As mantle modal mineralogy is unconstrained beneath Glacier Peak, bulk partition coefficients (D) for melting within the spinel peridotite field were used (Kelley et al., 2006; Workman and Hart, 2005) (Appendix C). REE patterns and equilibration pressures of parental magmas support this assumption.

The degree of melting (F) required to produce Whitechuck LKT from a PME-adjusted mantle sources is either 15% melting (F: 0.151±0.05) of a DMM source or 13.5% melting (F: 0.135 ±0.067).of an E-DMM source. Indian Pass CAB can be generated by 13.7% melting (F:0.137±0.030, bulk D from Workman and Hart (2005), or F: 0.137±0.026, bulk D from Kelley et al. (2006)) of a mantle source similar to that of Oregon Cascades sample WF021 (Ruscitto et al., 2010b).

Degrees of melting (above), input into the batch melting equation, were used to solve for the abundances of non-conservative trace elements and volatiles in the mantle source of parental magmas. The difference between these calculated abundances and those expected in the PME-corrected mantle source isolates the incompatible elements and volatiles attributable to the slab contribution. This provides a first-order constraint on the minimum H_2O present in the slab component and the amount of subduction component added to the mantle wedge. This modeling indicates that the Whitechuck LKT mantle source has been fluxed either with 0.34 wt. % subduction component (with the DMM initial source) or 0.30 wt. % subduction component (E-DMM initial source). The H_2O predicted to be present in the slab is either 0.28 wt. % (DMM) or 0.25 wt. % (E-DMM). Modeling indicates that the Indian Pass CAB mantle source has been fluxed wither with 0.28 or 0.29 wt. % subduction component containing either 0.21 or 0.22 wt.

% H_2O, depending on whether bulk partition coefficients are from Salters and Stracke (2004) or Workman and Hart (2005).

Conclusions

H_2O contents measured at primitive magmas in the southern Garibaldi Belt, at Mount Baker and Glacier Peak, and corrected for post-entrapment crystallization, range between 2.0 and 2.3 wt. %, overlapping the global range for arc volcanoes. Due to uncertain extents of crustal interaction, H_2O contents at Mount Baker cannot be related to parental values. Glacier Peak primitive LKT (Whitechuck cinder cone) and CAB (Indian Pass cinder cone) lavas, contain minimum H_2O contents of 2.0 and 2.2 wt. %, respectively. Parental magmas (in equilibrium with mantle olivine [Fo90]), are expected to have 1.7 and 2.0 wt. % H_2O. Trace element, isotopic data, and modeling suggest that these H_2O concentrations are unlikely to be the result of crustal interaction, decompression melting of the mantle wedge or of decompression melting of hydrous phases within the mantle wedge.

I conclude that both LKT and CAB at Glacier Peak are the result of between 13 and 15% fluid-fluxed melting of a compositionally heterogeneous source, last equilibrated near the base of the crust, with maximum temperatures at or near the dry peridotite solidus. Source heterogeneities likely include a MORB-like component and an OIB-like component. Minimum H_2O contents suggested in the slab component are between 0.21 and 0.28 wt %. This is in contrast to southern regions of the Cascade arc, where LKT magmas are considered as the result of dry decompression melting of a MORB-like source, though it is consistent with the more pronounced arc signature seen in this northern LKT.

Works Cited

Anderson, A.T., 1974, Evidence for a picritic, volatile-rich magma beneath Mt Shasta, California: Journal of Petrology, v. 15, p. 243-267.

Bacon, C.R., 1997, Primitive magmas at five Cascade volcanic fields; melts from hot, heterogeneous sub-arc mantle: Canadian Mineralogist, v. 35, Part 2, p. 397-423.

Baggerman, T.D., and DeBari, S., 2010, The generation of a diverse suite of Late Pleistocene and Holocene basalt through dacite lavas from the northern Cascade arc at Mount Baker, Washington: Contributions to Mineralogy and Petrology, p. 1-25.

Basaltic Volcanism Study Project, 1981, Basaltic Volcanism on the Terrestrial Planets, Pergamon Press.

Blundy, J., and Cashman, K., 2005, Rapid decompression-driven crystallization recorded by melt inclusions from Mount St. Helens Volcano: Geology [Boulder], v. 33, p. 793-796.

Borg, L.E., Clynne, M.A., and Bullen, T.D., 1997, The variable role of slab-derived fluids in the generation of a suite of primitive calc-alkaline lavas from the southernmost Cascades, California: Canadian mineralogist, v. 35, p. 425-452.

Borisov, A.A., and Shapkin, A.I., 1990, A new empirical equation rating Fe^{3+}/Fe^{2+} in magmas to their composition, oxygen fugacity, and temperature: Geochemistry International, v. 27, p. 111-116.

Brown, E.H., 1987, Structural geology and accretionary history of the Northwest Cascades system, Washington and British Columbia: Geological Society of America Bulletin, v. 99, p. 201-214.

Carroll, M.K., and Rutherford, M.J., 1988, Sulfur speciation in hydrous experimental glasses of varying oxidation state--results from measured wavelength shifts of sulfur X-rays: American Mineralogist, v. 73, p. 845-9.

Cervantes, P., and Wallace, P.J., 2003, Role of H2O in subduction-zone magmatism: New insights from melt inclusions in high-Mg basalts from central Mexico: Geology, v. 31, p. 235.

Conrey, R.M., Sherrod, D.R., Hooper, P.R., and Swanson, D.A., 1997, Diverse primitive magmas in the Cascade arc, northern Oregon and southern Washington: Canadian mineralogist, v. 35, p. 367-396.

Danyushevsky, L.V., Dela-Pasqua, F.N., and Sokolov, S., 2000, Re-equilibration of melt inclusions trapped by magnesian olivine phenocrysts from subduction: Contributions to Mineralogy & Petrology, v. 138, p. 68.

Danyushevsky, L.V., McNeill, A.W., and Sobolev, A.V., 2002, Experimental and petrological studies of melt inclusions in phenocrysts from mantle-derived magmas: an overview of techniques, advantages and complications: Chemical Geology, v. 183, p. 5.

Danyushevsky, L.V., and Plechov, P., 2008, Petrolog3: Integrated software for modelling crystallisation processes.

DeBari, S.M., Taylor, D.D., and Nelson, B., submitted, Mafic magmas from Glacier Peak, northern Cascade arc, and the role of magma mixing in generating high-Mg andesites: Contributions to Mineralogy & Petrology.

Dixon, J.E., 1991, Degassing history of water, sulfur, and carbon in submarine lavas from Kilauea Volcano, Hawaii: Journal of Geology, v. 99, p. 371-394.

—, 2001, Volatiles in basaltic glasses from Loihi Seamount, Hawaii; evidence for a relatively dry plume component: Journal of Petrology, v. 42, p. 627-654.

Dixon, J.E., Leist, L., Langmuir, C., and Schilling, J.G., 2002, Recycled dehydrated lithosphere observed in plume-influenced mid-ocean-ridge basalt: Nature, v. 420, p. 385-389.

Dixon, J.E., and Pan, V., 1995, Determination of the molar absorptivity of dissolved carbonate in basanitic glass: American Mineralogist, v. 80, p. 1339-1342.

Donovan, J.J., and Tingle, T.N., 1996, An Improved Mean Atomic Number Background Correction for Quantitative Microanalysis: Microscopy and Microanalysis, v. 2, p. 1-7.

Fumagalli, P., and Poli, S., 2005, Experimentally determined phase relations in hydrous peridotites to 6.5 GPa and their consequences on the dynamics of subduction zones: Journal of Petrology, v. 46, p. 555.

Fyfe, W.S., and McBirney, A.R., 1975, Subduction and the structure of andesitic volcanic belts: American Journal of Science, v. Vol. 275-A, p. 285-297.

Gaetani, G.A., and Watson, E.B., 2000, Open system behavior of olivine-hosted melt inclusions: Earth and Planetary Science Letters, v. 183, p. 27-41.

Gill, J.B., 1981, Orogenic Andesites and Plate Tectonics, Minerals and Rocks, Volume Volume 16: Berlin, Heidelberg, New York, Springer-Verlag.

Green, N.L., 1988, Basalt-basaltic andesite mixing at Mount Baker volcano, Washington, I. Estimation of mixing conditions: Journal of Volcanology and Geothermal Research, v. 34, p. 251-265.

Green, N.L., and Harry, D.L., 1999, On the relationship between subducted slab age and arc basalt petrogenesis, Cascadia subduction system, North America: Earth and Planetary Science Letters, v. 171, p. 367-381.

Green, N.L., and Sinha, A.K., 2005, Consequences of varied slab age and thermal structure on enrichment processes in the sub-arc mantle of the northern Cascadia subduction system: Journal of Volcanology & Geothermal Research, v. 140, p. 107-132.

Grove, T.L., Chatterjee, N., Parman, S.W., and Médard, E., 2006, The influence of H2O on mantle wedge melting: Earth and Planetary Science Letters, v. 249, p. 74-89.

Grove, T.L., Parman, S.W., Bowring, S.A., Price, R.C., and Baker, M.B., 2002, The role of an H_2O-rich fluid component in the generation of primitive basaltic andesites: Contributions to Mineralogy & Petrology, v. 142, p. 375.

Guffanti, M., and Weaver, C.S., 1988, Distribution of late Cenozoic volcanic vents in the Cascade Range; volcanic arc segmentation and regional tetonic considerations: Journal of Geophysical Research, v. 93, p. 6513-6529.

Hacker, B.R., 2008, H2O subduction beyond arcs: Geochem. Geophys. Geosyst, v. 9, p. Q03001.

Hart, W.K., Aronson, J.L., and Mertzman, S.A., 1984, Areal distribution and age of low-K, high-alumina olivine tholeiite magmatism in the northwestern Great Basin: Geological Society of America Bulletin, v. 95, p. 186-195.

Hildreth, W., Fierstein, J., and Lamphere, M., 2003, Eruptive history and geochronology of the Mount Baker volcanic field, Washington: Geological Society of America Bulletin, v. 115, p. 729.

Hirschmann, M.M., 2000, Mantle solidus: experimental constraints and the effects of peridotite composition: Geochemistry Geophysics Geosystems, v. 1, p. 1042-26.

Holloway, J.R., and Burnham, C.W., 1972, Melting relations of basalt with equilibrium water pressure less than total pressure: Journal of Petrology, v. 13, p. 1.

Hughes, S.S., and Taylor, E.M., 1986, Geochemistry, petrogenesis, and tectonic implications of central High Cascade mafic platform lavas: Geological Society of America Bulletin, v. 97, p. 1024-1036.

Jamtveit, B., Brooker, R., Brooks, K., Larsen, L.M., and Pedersen, T., 2001, The water content of olivines from the North Atlantic Volcanic Province: Earth and Planetary Science Letters, v. 186, p. 401-415.

Johnson, E.R., Wallace, P.J., Delgado Granados, H., Manea, V.C., Kent, A.J.R., Bindeman, I.N., and Donegan, C.S., 2009, Subduction-related Volatile Recycling and Magma Generation beneath Central Mexico: Insights from Melt Inclusions, Oxygen Isotopes and Geodynamic Models: J. Petrology, v. 50, p. 1729-1764.

Katz, R.F., Spiegelman, M., and Langmuir, C.H., 2003, A new parameterization of hydrous mantle melting: Geochem. Geophys. Geosyst, v. 4, p. 1073.

Kelley, K.A., Plank, T., Grove, T.L., Stolper, E.M., Newman, S., and Hauri, E., 2006, Mantle melting as a function of water content beneath back-arc basins: Journal of Geophysical Research, v. 111.

Kelley, K.A., Plank, T., Newman, S., Stolper, E.M., Grove, T.L., Parman, S., and Hauri, E.H., 2010, Mantle melting as a function of water content beneath the Mariana Arc: Journal of Petrology, v. 51, p. 1711-1738.

Kent, A.J.R., 2008, Melt inclusions in basaltic and related volcanic rocks: Reviews in Mineralogy and Geochemistry, v. 69, p. 273-331.

Lange, R.A., Frey, H.M., and Hector, J., 2009, A thermodynamic model for the plagioclase-liquid hygrometer/thermometer: American Mineralogist, v. 94, p. 494.

Le Voyer, M., Rose-Koga, E.F., Shimizu, N., Grove, T.L., and Schiano, P., 2010, Two Contrasting H2O-rich Components in Primary Melt Inclusions from Mount Shasta: Journal of Petrology, v. 51, p. 1571-1595.

Lee, C.-T.A., Luffi, P., Plank, T., Dalton, H., and Leeman, W.P., 2009, Constraints on the depths and temperatures of basaltic magma generation on Earth and other terrestrial planets using new thermobarometers for mafic magmas: Earth and Planetary Science Letters, v. 279, p. 20-33.

Leeman, W.P., Lewis, J.F., Evarts, R.C., Conrey, R.M., and Streck, M.J., 2005a, Petrologic constraints on the thermal structure of the Cascades arc: Journal of Volcanology & Geothermal Research, v. 140, p. 67-105.

Leeman, W.P., Smith, D.R., Hildreth, W., Palacz, Z.A., and Rogers, N.W., 1990, Compositional diversity of late Cenozoic basalts in a transect across the southern Washington Cascades: Implications for subduction zone magmatism: Journal of Geophysical Research, v. 95, p. 19.

Leeman, W.P., Streck, M.J., Chesley, J.T., and Tonarini, S., 2005b, Evidence for magma-mixing and disequilibrium in 'primitive' basaltic andesites from Mount Shasta, Northern California: Eos, Transactions, American Geophysical Union, v. 86, p. v11a.

McBirney, A.R., 1969, Compositional variations in Cenozoic calc-alkaline suites of Central America, *in* McBirney, A.R., ed., Andesite Conference, Proceedings, Volume 65: United States, Oregon Department of Geology and Mineral Industries : Portland, OR, United States, p. 185-189.

McCrory, P.A., Blair, J.L., Oppenheimer, D.H., and Walter, S.R., 2004, Depth to the Juan De Fuca slab beneath the Cascadia subduction margin a 3-D model for sorting earthquakes: Reston, VA, U.S. Dept. of the Interior, U.S. Geological Survey.

Médard, E., and Grove, T., 2008, The effect of H_2O on the olivine liquidus of basaltic melts: experiments and thermodynamic models: Contributions to Mineralogy & Petrology, v. 155, p. 417-432.

Mooney, W.D., and Weaver, C.S., 1989, Regional crustal structure and tectonics of the Pacific coastal states; California, Oregon, and Washington: Memoir - Geological Society of America, v. 172, p. 129-161.

Moore, N.E., and DeBari, S.M., submitted, Origin and geochemical evolution of mafic magmas from Mount Baker in the northern Cascade arc, Washington : probes into mantle and crustal processes: Contributions to Mineralogy & Petrology.

Newman, S., and Lowenstern, J.B., 2002, VolatileCalc: a silicate melt H2O–CO2 solution model written in Visual Basic for excel: Computers & Geosciences, v. 28, p. 597.

Parsons, T., Trehu, A.M., Luetgert, J.H., Miller, K., Kilbride, F., Wells, R.E., Fisher, M.A., Flueh, E., ten Brink, U.S., and Christensen, N.I., 1998, A new view into the Cascadia subduction zone and volcanic arc: Implications for earthquake hazards along the Washington margin: Geology, v. 26, p. 199-202.

Poli, S., and Schmidt, M.W., 2002, Petrology of Subducted Slabs: Annual Review of Earth & Planetary Sciences, v. 30, p. 207.

Portnyagin, M., Almeev, R., Matveev, S., and Holtz, F., 2008, Experimental evidence for rapid water exchange between melt inclusions in olivine and host magma: Earth and Planetary Science Letters, v. 272, p. 541-552.

Portnyagin, M., Hoernle, K., Plechov, P., Mironov, N., and Khubunaya, S., 2007, Constraints on mantle melting and composition and nature of slab components in volcanic arcs from volatiles (H2O, S, Cl, F) and trace elements in melt inclusions from the Kamchatka Arc: Earth and Planetary Science Letters, v. 255, p. 53-69.

Reiners, P.W., Hammond, P.E., McKenna, J.M., and Duncan, R.A., 2000, Young basalts of the central Washington Cascades, flux melting of the mantle, and trace element signatures of primary arc magmas: Contributions to Mineralogy and Petrology, v. 138, p. 249-264.

Rowe, M.C., Kent, A.J.R., and Nielsen, R.L., 2007, Determination of sulfur speciation and oxidation state of olivine hosted melt inclusions: Chemical Geology, v. 236, p. 303-322.

—, 2009, Subduction Influence on Oxygen Fugacity and Trace and Volatile Elements in Basalts Across the Cascade Volcanic Arc: J. Petrology, v. 50, p. 61-91.

Ruscitto, D., Wallace, P., and Kent, A., 2010a, Revisiting the compositions and volatile contents of olivine-hosted melt inclusions from the Mount Shasta region: implications for the formation of high-Mg andesites: Contributions to Mineralogy and Petrology, p. 1-24.

Ruscitto, D.M., Wallace, P.J., Johnson, E.R., Kent, A.J.R., and Bindeman, I.N., 2010b, Volatile contents of mafic magmas from cinder cones in the Central Oregon High Cascades: Implications for magma formation and mantle conditions in a hot arc: Earth & Planetary Science Letters, v. 298, p. 153-161.

Salters, V.J.M., and Stracke, A., 2004, Composition of the depleted mantle: Geochem. Geophys. Geosyst., v. 5, p. Q05B07.

Schmidt, M.E., Grunder, A.L., and Rowe, M.C., 2008, Segmentation of the Cascade Arc as indicated by Sr and Nd isotopic variation among diverse primitive basalts: Earth and Planetary Science Letters, v. 266, p. 166-181.

Sisson, T.W., and Bronto, S., 1998, Evidence for pressure-release melting beneath magmatic arcs from basalt at Galunggung, Indonesia: Nature, v. 391, p. 883.

Sisson, T.W., and Grove, T.L., 1993, Experimental investigations of the role of H2O in calc-alkaline differentiation and subduction zone magmatism: Contributions to Mineralogy and Petrology, v. 113, p. 143-166.

Sisson, T.W., and Layne, G.D., 1993, H2O in basalt and basaltic andesite glass inclusions from four subduction-related volcanoes: Earth and Planetary Science Letters, v. 117, p. 619-635.

Smith, P.M., and Asimow, P.D., 2005, Adiabat_1ph: A new public front-end to the MELTS, pMELTS, and pHMELTS models: Geochemistry, Geophysics, Geosystems, v. 6, p. 2004GC000816.

Sobolev, A.V., 1996, Melt inclusions in minerals as a source of principle petrological information: Petrology, v. 4, p. U1-U1.

Sobolev, A.V., and Chaussidon, M., 1996, H2O concentrations in primary melts from supra-subduction zones and mid-ocean ridges: Implications for H2O storage and recycling in the mantle: Earth and Planetary Science Letters, v. 137, p. 45-55.

Stolper, E., and Newman, S., 1994, The role of water in the petrogenesis of Mariana trough magmas: Earth and Planetary Science Letters, v. 121, p. 293-325.

Streck, M.J., Leeman, W.P., and Chesley, J., 2007, High-magnesian andesite from Mount Shasta: A product of magma mixing and contamination, not a primitive mantle melt: Geology, v. 35, p. 351-354.

Sugawara, T., 2000, Empirical relationships between temperature, pressure, and MgO content in olivine and pyroxene saturated liquid: J. Geophys. Res., v. 105, p. 8457-8472.

Sun, S.S., and McDonough, W., 1989, Chemical and isotopic systematics of oceanic basalts: implications for mantle composition and processes: Geological Society, London, Special Publications, v. 42, p. 313.

Tabor, R.W., and Crowder, D.F., 1969, On batholiths and volcanoes; intrusion and eruption of late Cenozoic magmas in the Glacier Peak area, North Cascades, Washington: United States, U. S. Geological Survey : Reston, VA, United States.

Taylor, D.D., 2001, Petrology and geochemistry of mafic lavas near Glacier Peak, North Cascades, Washington: Bellingham, Western Washington University.

Toplis, M.J., 2005, The thermodynamics of iron and magnesium partitioning between olivine and liquid: criteria for assessing and predicting equilibrium in natural and experimental systems: Contributions to Mineralogy & Petrology, v. 149, p. 22-39.

van Keken, P.E., Hacker, B.R., Syracuse, E.M., and Abers, G.A., 2011, Subduction factory: 4. Depth-dependent flux of H2O from subducting slabs worldwide: J. Geophys. Res., v. 116, p. B01401.

Vigouroux, N., Wallace, P.J., and Kent, A.J.R., 2008, Volatiles in high-K magmas from the western Trans-Mexican volcanic belt: Evidence for fluid fluxing and extreme enrichment of the mantle wedge by subduction processes: Journal of Petrology, v. 49, p. 1589-1618.

Wallace, P.J., 2005, Volatiles in subduction zone magmas: concentrations and fluxes based on melt inclusion and volcanic gas data: Journal of Volcanology & Geothermal Research, v. 140, p. 217-240.

Wallace, P.J., and Carmichael, I.S.E., 1994, S speciation in submarine basaltic glasses as determined by measurements of SKalpha X-ray wavelength shifts: American Mineralogist, v. 79, p. 161-167.

Wilson, D.S., 1988, Tectonic History of the Juan de Fuca Ridge Over the Last 40 Million Years: J. Geophys. Res., v. 93, p. 11863-11876.

Workman, R.K., and Hart, S.R., 2005, Major and trace element composition of the depleted MORB mantle (DMM): Earth and Planetary Science Letters, v. 231, p. 53-72.

Wysoczanski, R., and Tani, K., 2006, Spectroscopic FTIR imaging of water species in silicic volcanic glasses and melt inclusions: An example from the Izu-Bonin arc: Journal of Volcanology & Geothermal Research, v. 156, p. 302-314.

Yoder Jr, H., and Kushiro, I., 1969, Melting of a hydrous phase: phlogopite: American Journal of Science, v. 267, p. 558.

Table 1: Major and Trace Element Data Corrected for Post-Entrapment Crystallization

Whitechuck LKT (location:48°03'02",-121°09'42")

Sample	WC 002_1	1s.e.	WC 002_2	1s.e.	WC 003	1s.e.	WC 007	1s.e.	WC 008	1s.e.	WC 013	1s.e.	WC 014	1s.e.	WC 017	1s.e.
SiO_2	50.86	0.32	50.71	0.15	50.05	0.31	51.44	0.24	50.75	0.11	50.28	0.21	50.98	0.66	50.65	0.25
TiO_2	1.16	0.04	1.12	0.05	1.13	0.05	1.29	0.05	1.10	0.08	1.14	0.05	1.13	0.06	1.15	0.07
Al_2O_3	18.59	0.17	18.72	0.11	19.21	0.21	18.75	0.16	18.22	0.11	18.83	0.11	18.32	0.48	18.52	0.07
FeO^T	7.93	0.08	7.96	0.13	7.92	0.09	7.51	0.06	8.02	0.03	8.04	0.12	7.99	0.61	8.01	0.08
MnO	0.15	0.01	0.15	0.01	0.13	0.01	0.14	0.01	0.13	0.01	0.13	0.01	0.14	0.02	0.14	0.01
MgO	6.82	0.26	6.83	0.13	6.71	0.06	6.04	0.18	6.84	0.12	6.89	0.05	6.80	0.79	6.92	0.05
CaO	10.32	0.07	10.32	0.04	10.54	0.03	10.49	0.05	10.69	0.03	10.48	0.04	10.13	1.12	10.39	0.02
Na_2O	3.43	0.15	3.44	0.13	3.50	0.09	3.52	0.06	3.46	0.05	3.43	0.09	3.72	0.40	3.47	0.14
K_2O	0.39	0.01	0.40	0.01	0.44	0.01	0.47	0.01	0.44	0.02	0.43	0.01	0.44	0.02	0.41	0.01
P_2O_5	0.22	0.01	0.21	0.01	0.22	0.01	0.23	0.00	0.22	0.02	0.21	0.01	0.21	0.00	0.20	0.01
S [a]	1470	60	1480	50	1600	10	1600	60	1590	10	1700	40	1690	60	1320	40
Cl	923	20	926	30	950	40	973	30	941	30	906	40	1011	170	917	40
H_2O [b]	1.5	0.2	1.8	0.1	0.5	0.1	2.0	0.1	1.9	0.1	1.1	019	0.6	0.1	1.9	0.1
CO_2 [b]	612	68	821	50	334	64	650	44	755	47	244	20	281	44	508	37
T (°C) [c]	1131		1127		1160		1100		1121		1141		1158		1121	
P(MPa)[d]	154		202		74		190		200		68		67		146	
HostFo#	86		86		86		85		86		86		86		86	
%Ol	0.4		0.1		0.7		4.7		1.9		3.7		4.6		0.3	
fO2 +ΔFMQ	1.4		1.4		1.0		1.0		1.4		1.1		1.1		1.3	
Mg #	65		65		64		63		64		65		64		65	

Whitechuck LKT *Indian Pass CAB(location:47°59'58",-121°06'54")*

Sample	WC 020_1	1s.e.	WC 020_2	1s.e.	WC 023	1s.e.	IP 001	1s.e.	IP 003_1	1s.e.	IP 005	1s.e.	IP 016	1s.e.	IP 020	1s.e.
SiO_2	50.76	0.24	50.31	0.06	50.05	0.26	50.38	0.27	49.35	0.15	53.72	0.55	50.19	0.23	50.10	0.34
TiO_2	1.17	0.06	1.13	0.05	1.13	0.06	1.38	0.11	1.55	0.03	2.09	0.02	1.49	0.05	1.42	0.04
Al_2O_3	18.47	0.53	18.97	0.21	17.82	0.15	17.55	0.08	17.70	0.08	15.74	0.08	17.88	0.19	17.52	0.29
FeO^T	8.03	0.30	8.01	0.19	8.62	0.04	7.23	0.08	7.21	0.07	7.01	0.10	7.01	0.07	7.22	0.24
MnO	0.13	0.01	0.12	0.01	0.16	0.00	0.11	0.01	0.10	0.01	0.11	0.02	0.12	0.00	0.10	0.01
MgO	6.90	0.51	6.77	0.18	7.36	0.22	6.97	0.34	7.24	0.23	6.59	0.06	6.37	0.06	7.16	0.57
CaO	10.41	0.02	10.22	0.02	10.14	0.05	10.59	0.05	10.52	0.06	8.07	0.07	10.80	0.04	10.91	0.04
Na_2O	3.36	0.24	3.65	0.04	3.90	0.12	4.28	0.14	4.60	0.14	4.00	1.09	4.52	0.16	4.11	0.22
K_2O	0.41	0.03	0.45	0.01	0.47	0.01	0.83	0.03	0.98	0.04	1.73	0.02	0.91	0.02	0.79	0.04
P_2O_5	0.21	0.01	0.23	0.02	0.22	0.01	0.53	0.02	0.61	0.01	0.78	0.01	0.56	0.00	0.53	0.01
S [a]	1650	70	1740	10	1200	40	2960	20	2860	80	89	10	2550	30	3320	90
Cl	921	30	929	30	917	40	446	30	520	10	711	10	447	30	418	40
H_2O [b]	1.3	0.1	0.8	0.1	1.1	0.2	2.2	0.3	1.4	0.9	1.1	0.1	1.6	0.1	1.7	0.2
CO_2 [b]	430	34	155	16	547	98	1724	259	387	48	b.d.	b.d.	1233	88	1200	156
T (°C) [c]	1138		1149		1154		1124		1140		1137		1123		1137	
P(MPa)[d]	114		44		133		374		89		82		223		238	
HostFo#	86		86		86		88		89		88		87		88	
%Ol	4.0		8.2		3.5		3.0		3.7		5.2		0.6		5.1	
fO2 +ΔFMQ	1.0		0.8		0.8		1.4		1.4		---		1.5		1.5	
Mg #	65		64		64		68		69		67		67		69	

Table 1 (continued): Major and Trace Element Data Corrected for Post-Entrapment Crystallization

Schreiber's Meadow CAB (location:48°69'62",-121°79'37")

Sample	SM 001	*1s.e.*	SM 005	*1s.e.*	SM 025	*1s.e.*	SM 027	*1s.e.*	SM 029	*1s.e.*	SM 030	*1s.e.*	SM 032	*1s.e.*
SiO_2	52.74	*0.14*	51.85	*0.28*	49.28	*0.59*	51.74	*0.48*	52.65	*0.83*	57.12	*0.42*	52.99	*0.43*
TiO_2	1.26	*0.02*	1.29	*0.05*	0.67	*0.04*	1.33	*0.08*	1.82	*0.04*	1.93	*0.08*	1.22	*0.04*
Al_2O_3	17.56	*0.20*	18.94	*0.09*	18.75	*0.64*	18.73	*0.41*	16.53	*0.42*	17.14	*0.06*	18.79	*0.36*
FeO^T	8.73	*0.16*	6.51	*0.14*	10.37	*0.14*	7.47	*0.08*	9.06	*0.27*	6.48	*0.15*	6.49	*0.06*
MnO	0.15	*0.01*	0.10	*0.02*	0.18	*0.01*	0.17	*0.01*	0.17	*0.01*	0.12	*0.01*	0.13	*0.01*
MgO	5.11	*0.02*	5.70	*0.13*	6.25	*0.39*	4.63	*0.07*	5.06	*0.47*	3.35	*0.08*	4.96	*0.03*
CaO	9.32	*0.05*	10.13	*0.32*	11.27	*0.03*	10.17	*0.02*	7.70	*0.08*	5.78	*0.06*	10.34	*0.04*
Na_2O	4.41	*0.10*	4.17	*0.16*	2.47	*0.09*	4.51	*0.21*	4.99	*0.11*	5.17	*0.26*	3.75	*0.47*
K_2O	0.35	*0.02*	0.78	*0.17*	0.40	*0.01*	0.79	*0.02*	1.34	*0.05*	2.10	*0.02*	0.83	*0.01*
P_2O_5	0.20	*0.01*	0.41	*0.01*	0.16	*0.01*	0.33	*0.00*	0.52	*0.01*	0.69	*0.01*	0.38	*0.01*
S [a]	983	*10*	1530	*30*	665	*30*	1480	*20*	1200	*40*	168	*80*	1480	*40*
Cl	205	*20*	456	*40*	218	*10*	477	*20*	424	*20*	456	*30*	453	*20*
H_2O [b]	0.97	*0.10*	2.27	*0.15*	2.05	*0.20*	1.82	*0.22*	1.34	*0.09*	0.76	*0.08*	1.70	*0.10*
CO_2 [b]	167	*18*	870	*57*	276	*27*	624	*76*	358	*23*	b.d.		410	*25*
T (°C) [c]	1105		1089		1100		1074		1094		1070		1082	
P(MPa)[d]	50		255		112		172		97		6		121	
HostFo#	80		86		80		81		80		80		84	
%Ol add.	7.0		6.9		5.0		2.6		1.4		0.9		1.5	
fO2 +ΔFMQ	---		---		1.0		1.1		0.9		0.7		1.0	
Mg#	56		65		56		57		54		52		62	

Major elements in wt. %, CO_2, S, Cl in ppm. Unless otherwise noted, analyses performed at University of Oregon CAMCOR lab. Fe reported as total FeO^T [a]Analysis performed at Washington State University [b]Performed with FTIR at University of Oregon. [c] Calculated as per (Sugawara, 2000), corrected as per (Médard and Grove, 2008) [d] Entrapment pressure calculated with VolatileCalc (Newman and Lowenstern, 2002)

Table 1 (continued): Major and Trace Element Data Corrected for Post-Entrapment Crystallization

Whitechuck

Sample	WC 002_1	1s.e.	WC 002_2	1s.e.	WC 003	1s.e.	WC 007	1s.e.	WC 008	1s.e.	WC 013	1s.e.	WC 017	1s.e.	WC 020_1	1s.e.	WC 020_2	1s.e.	WC 023	1s.e.
Ba	77	*1*	79	*2*	90	*2*	103	*3*	79	*4*	95	*6*	79	*4*	100	*5*	98	*3*	106	*3*
Ce	15.4	*0.4*	16.5	*0.6*	17.5	*0.8*	18.5	*1.0*	12.5	*1.0*	16.8	*0.7*	14.7	*0.6*	16.7	*0.9*	18.0	*2.1*	17.6	*0.6*
Dy	2.8	*0.4*	2.8	*0.8*	3.5	*0.3*	3.7	*0.6*	-	-	2.6	*0.3*	2.8	*0.1*	3.9	*0.6*	3.0	*0.6*	-	-
Er	2.0	*0.2*	1.9	*0.2*	1.1	*0.2*	1.4	*0.0*	3.0	*0.8*	1.5	*0.3*	1.4	*0.2*	1.3	*0.3*	2.2	*0.3*	2.1	*0.3*
Eu	1.0	*0.1*	1.0	*0.3*	0.9	*0.1*	1.4	*0.1*	-	-	1.0	*0.1*	0.9	*0.1*	0.7	*0.2*	1.1	*0.1*	1.1	*0.1*
Gd	2.9	*0.7*	3.4	*0.6*	3.0	*0.3*	4.1	*0.8*	-	-	3.0	*0.3*	2.3	*0.2*	3.4	*0.4*	2.5	*0.6*	2.7	*0.5*
Hf	1.9	*0.2*	1.7	*0.2*	1.8	*0.2*	1.4	*0.1*	-	-	1.4	*0.2*	1.7	*0.2*	3.4	*0.9*	3.8	*0.5*	2.0	*0.2*
La	5.1	*0.3*	5.1	*0.4*	4.9	*0.2*	6.0	*0.5*	-	-	5.9	*0.3*	4.6	*0.1*	5.4	*0.6*	6.0	*0.5*	5.9	*0.2*
Nb	1.1	*0.1*	1.0	*0.0*	1.1	*0.1*	1.0	*0.1*	-	-	1.1	*0.1*	1.1	*0.1*	1.1	*0.2*	1.8	*0.1*	1.4	*0.1*
Nd	10.9	*0.4*	10.7	*0.3*	11.4	*0.8*	16.0	*1.3*	5.4	*1.0*	11.0	*0.5*	10.8	*1.0*	10.7	*0.7*	10.7	*1.6*	11.0	*0.8*
Pb	2.9	*0.3*	2.0	*0.3*	2.4	*0.2*	3.4	*0.1*	3.7	*0.6*	1.8	*0.3*	2.2	*0.3*	3.6	*0.6*	3.7	*0.5*	3.1	*0.2*
Pr	2.8	*0.2*	2.5	*0.1*	2.5	*0.2*	2.7	*0.1*	1.9	*0.6*	2.2	*0.1*	2.2	*0.1*	2.5	*0.2*	2.4	*0.2*	2.8	*0.2*
Rb	3.6	*0.2*	2.2	*0.2*	4.2	*0.2*	3.7	*0.2*	-	-	3.7	*0.2*	2.6	*0.4*	4.9	*0.5*	5.0	*0.7*	4.7	*0.6*
Sc	31.3	*1.9*	30.3	*0.6*	32.5	*1.8*	32.0	*1.4*	84.0	*2.1*	29.0	*1.0*	23.2	*1.7*	40.1	*4.5*	41.5	*4.3*	29.6	*1.5*
Sm	2.6	*0.3*	2.5	*0.2*	3.2	*0.3*	3.8	*0.5*	-	-	-	-	-	-	-	*0.9*	3.4	*0.7*	2.7	*0.3*
Sr	540	*9*	534	*17*	530	*13*	533	*18*	457	*35*	553	*16*	535	*14*	539	*16*	549	*11*	514	*9*
Ta	-	-	0.1	*0.0*	-	-	-	-	-	-	-	-	-	-	-	-	0.2	*0.0*	-	-
Th	0.7	*0.1*	0.6	*0.2*	0.7	*0.1*	0.7	*0.1*			0.6	*0.0*	-	-	1.0	*0.3*	0.6	*0.1*	0.6	*0.1*
Ti[a]	6550	*110*	6480	*110*	6830	*160*	7380	*250*	5220	*490*	6390	*160*	6130	*260*	6470	*160*	7550	*200*	6710	*130*
U	0.1	*0.0*	-	-	0.2	*0.1*	0.3	*0.1*	-	-	0.1	*0.0*	0.2	*0.0*	0.3	*0.0*	0.2	*0.1*	0.2	*0.0*
V	209	*7*	217	*8*	249	*9*	232	*11*	266	*22*	221	*9*	211	*15*	246	*12*	252	*9*	211	*10*
Y	16.4	*0.4*	18.1	*0.2*	15.9	*0.5*	18.2	*0.5*	14.3	*1.6*	14.4	*1.4*	15.3	*0.4*	21.0	*1.0*	18.3	*0.4*	17.1	*0.3*
Yb	1.7	*0.2*	2.4	*0.6*	1.4	*0.2*	1.6	*0.3*	-	-	1.6	*0.2*	1.9	*0.2*	3.1	*0.7*	2.4	*0.8*	1.9	*0.2*
Zr	75	*1.5*	77	*4.3*	74	*2.1*	80	*1.4*	75	*5.1*	68	*2.1*	74	*2.4*	83	*2.9*	87	*3.0*	75	*1.6*

All trace elements in ppm. Unless specified, all TE analyses performed with LA-ICP-MS and Oregon State University. [a] Calculated from TiO_2 analyzed with EPMA at University of Oregon.

Table 1 (continued): Major and Trace Element Data Corrected for Post-Entrapment Crystallization

Indian Pass CAB					*Schreiber's Meadow CAB*									
Sample	IP 0031–	*1s.e.*	IP 016	*1s.e.*	SM 025	*1s.e.*	SM 027	*1s.e.*	SM 029	*1s.e.*	SM 030	*1s.e.*	SM 032	*1s.e.*
Ba	416	*7*	344	*9*	201	*12*	258	*15*	382	*19*	549	*23*	247	*10*
Ce	68.3	*2.1*	48.8	*2.2*	12.1	*0.8*	21.0	*1.1*	44.1	*2.5*	58.4	*3.0*	26.9	*1.6*
Dy	3.0	*0.3*	3.1	*0.4*	2.1	*0.3*	1.8	*0.2*	7.5	*0.6*	5.6	*1.0*	1.5	*0.5*
Er	1.2	*0.5*	2.7	*0.5*	0.7	*0.2*	-	-	4.0	*0.3*	4.3	*0.3*	2.0	*0.7*
Eu	1.9	*0.3*	1.9	*0.1*	-	-	1.1	*0.1*	2.3	*0.2*	1.6	*0.1*	0.9	*0.2*
Gd	4.0	*0.9*	4.0	*0.4*	-	-	4.6	*1.2*	5.9	*0.6*	5.2	*0.7*	1.7	*0.2*
Hf	2.6	*0.1*	2.5	*0.3*	1.1	*0.2*	-	-	4.6	*0.3*	5.0	*0.3*	2.8	*0.2*
La	23.3	*1.4*	20.8	*0.7*	4.0	*0.3*	8.4	*0.6*	19.8	*0.8*	23.4	*1.1*	10.8	*0.6*
Nb	7.7	*0.5*	6.2	*0.4*	1.4	*0.2*	3.3	*0.5*	9.1	*0.6*	12.6	*0.6*	5.4	*0.3*
Nd	30.2	*1.6*	24.3	*1.2*	8.2	*0.6*	12.8	*1.1*	24.9	*1.2*	30.9	*1.2*	16.1	*1.5*
Pb	5.0	*0.2*	4.3	*0.4*	2.4	*0.1*	1.3	*0.2*	5.0	*0.2*	7.8	*0.7*	2.8	*0.1*
Pr	7.7	*0.3*	6.2	*0.3*	1.0	*0.1*	1.6	*0.2*	6.6	*0.5*	7.2	*0.4*	2.6	*0.2*
Rb	9.2	*0.3*	7.3	*0.7*	6.5	*0.2*	5.1	*0.3*	16.0	*0.5*	40.8	*1.6*	5.4	*0.5*
Sc	24.8	*2.2*	24.9	*1.0*	28.7	*1.6*	31.9	*1.5*	32.1	*2.4*	20.2	*2.1*	26.5	*1.0*
Sm	5.1	*0.8*	5.3	*0.5*	1.6	*0.4*	2.1	*0.5*	7.1	*0.5*	5.5	*0.8*	2.8	*0.7*
Sr	1291	*32*	1191	*37*	753	*33*	509	*24*	470	*19*	388	*17*	526	*20*
Ta	0.4	*0.1*	0.3	*0.0*	-	-	2.0	*0.7*	0.5	*0.1*	1.1	*0.1*	-	-
Th	2.9	*0.4*	2.0	*0.1*	-	-	-	-	2.3	*0.1*	5.0	*0.7*	-	-
Ti[a]	8890	*130*	7810	*210*	3920	*270*	6980	*470*	10510	*770*	12000	*800*	6940	*440*
U	0.9	*0.1*	0.6	*0.1*	0.3	*0.1*	-	-	0.9	*0.1*	1.4	*0.2*	-	-
V	229	*10*	195	*7*	114	*5*	252	*10*	198	*4*	221	*9*	222	*4*
Y	14.4	*1.0*	16.4	*0.4*	8.4	*0.4*	19.5	*1.0*	35.1	*2.0*	34.7	*1.7*	17.2	*0.9*
Yb	0.9	*0.2*	1.2	*0.1*	1.2	*0.4*	2.2	*0.5*	1.8	*0.6*	2.0	*0.4*	-	-
Zr	127	*8.5*	117	*7.6*	36	*1.7*	100	*3.9*	252	*9.1*	270	*20.5*	107	*4.9*

All trace elements in ppm. Unless specified, all TE analyses performed with LA-ICP-MS and Oregon State University. [a] Calculated from TiO_2 analyzed with EPMA at University of Oregon. 1 s.e. (standard error)

Table 2: Host Olivine Compositions

Whitechuck LKT

Sample	WC 002	*1 s.e.*	WC 003	*1 s.e.*	WC 007	*1 s.e.*	WC 008	*1 s.e.*	WC 013	*1 s.e.*	WC 014	*1 s.e.*	WC 017	*1 s.e.*	WC 020	*1 s.e.*	WC 023	*1 s.e.*
SiO_2	40.22	*0.20*	39.11	*0.12*	40.04	*0.10*	39.64	*0.21*	40.39	*0.13*	40.34	*0.05*	40.19	*0.12*	40.30	*0.21*	40.36	*0.20*
MgO	45.40	*0.11*	45.47	*0.15*	44.73	*0.05*	45.08	*0.10*	45.09	*0.08*	45.06	*0.12*	44.98	*0.22*	45.49	*0.32*	45.60	*0.09*
FeO	13.63	*0.18*	13.69	*0.21*	14.40	*0.20*	13.61	*0.10*	13.50	*0.35*	13.54	*0.20*	13.37	*0.19*	13.69	*0.18*	13.45	*0.29*
CaO	0.17	*0.00*	0.17	*0.00*	0.17	*0.00*	0.17	*0.00*	0.18	*0.00*	0.17	*0.00*	0.17	*0.00*	0.17	*0.00*	0.17	*0.00*
MnO	0.20	*0.00*	0.21	*0.00*	0.22	*0.01*	0.21	*0.01*	0.20	*0.01*	0.20	*0.00*	0.20	*0.00*	0.20	*0.01*	0.20	*0.01*
Total	99.63		98.65		99.56		98.71		99.35		99.32		98.90		99.84		99.78	
Fo#	86		86		86		85		86		86		86		86		86	

Indian Pass CAB

Sample	IP 001	*1 s.e.*	IP 003	*1 s.e.*	IP 005	*1 s.e.*	IP 016	*1 s.e.*	IP 020	*1 s.e.*
SiO_2	40.51	*0.11*	40.64	*0.04*	40.23	*0.23*	40.54	*0.21*	40.60	*0.28*
MgO	47.07	*0.06*	47.39	*0.08*	46.03	*0.02*	46.57	*0.04*	46.83	*0.13*
FeO	11.50	*0.13*	10.76	*0.13*	12.24	*0.06*	11.90	*0.15*	11.14	*0.05*
CaO	0.14	*0.00*	0.14	*0.00*	0.17	*0.01*	0.15	*0.00*	0.15	*0.00*
MnO	0.16	*0.01*	0.15	*0.01*	0.18	*0.01*	0.17	*0.00*	0.16	*0.01*
Total	99.68		99.47		99.10		99.62		99.18	
Fo#	88		89		88		87		88	

Schreiber's Meadow CAB

Sample	SM 001	*1 s.e.*	SM 005	*1 s.e.*	SM 025	*1 s.e.*	SM 027	*1 s.e.*	SM 029	*1 s.e.*	SM 030	*1 s.e.*	SM 032	*1 s.e.*
SiO_2	39.82	*0.28*	40.39	*0.30*	38.60	*0.15*	38.98	*0.14*	38.22	*0.30*	39.07	*0.15*	39.77	*0.25*
MgO	41.67	*0.25*	45.69	*0.07*	40.66	*0.56*	42.16	*0.03*	41.21	*0.49*	40.88	*0.27*	44.00	*0.50*
FeO	18.51	*0.14*	12.95	*0.19*	18.40	*0.17*	17.12	*0.48*	18.25	*0.70*	18.45	*0.23*	14.89	*0.41*
CaO	0.18	*0.00*	0.17	*0.00*	0.23	*0.00*	0.19	*0.01*	0.18	*0.01*	0.20	*0.01*	0.17	*0.00*
MnO	0.31	*0.01*	0.22	*0.01*	0.30	*0.00*	0.28	*0.01*	0.31	*0.02*	0.31	*0.01*	0.23	*0.02*
Total	100.59		99.60		98.20		98.86		98.29		98.99		99.25	
Fo#	80		86		80		81		80		80		84	

All values reported in wt %. Olivine compositions analyzed with EPMA at University of Oregon

Table 3: Compositions corrected to mantle equilibrium (Fo_{90}) (Inclusion Mg#: ~73) and normalized to 100

Sample	WC 002_1	WC 002_2	WC 003	WC 007	WC 008	WC 013	WC 014	WC 017	WC 020_1	WC 020_2	WC 023	WC Avg
SiO_2	48.74	48.60	48.01	49.14	48.61	48.21	48.81	48.55	48.64	48.22	47.94	48.50
TiO_2	1.00	0.97	0.97	1.11	0.95	0.98	0.97	1.00	1.01	0.97	0.96	0.99
Al_2O_3	16.07	16.17	16.55	16.05	15.70	16.24	15.79	16.01	15.94	16.32	15.22	16.01
FeO	7.14	7.16	7.16	6.91	7.22	7.23	7.20	7.19	7.22	7.22	7.69	7.21
Fe_2O_3	1.22	1.22	1.21	1.14	1.23	1.23	1.22	1.23	1.23	1.22	1.31	1.23
MnO	0.13	0.13	0.12	0.12	0.11	0.11	0.12	0.12	0.11	0.10	0.14	0.12
MgO	11.52	11.56	11.54	11.16	11.65	11.66	11.62	11.61	11.65	11.65	12.40	11.64
CaO	8.92	8.92	9.08	8.98	9.21	9.04	8.73	8.98	8.99	8.79	8.66	8.94
Na_2O	2.96	2.97	3.01	3.01	2.98	2.96	3.21	3.00	2.90	3.14	3.33	3.04
K_2O	0.34	0.35	0.38	0.40	0.37	0.37	0.37	0.35	0.36	0.39	0.40	0.37
P_2O_5	0.19	0.18	0.19	0.20	0.19	0.18	0.18	0.17	0.18	0.20	0.18	0.18
H_2O	1.70	1.70	1.70	1.70	1.70	1.70	1.70	1.70	1.70	1.70	1.70	1.70
%Ol add	13.6	13.7	14.0	14.7	14.0	13.9	14.0	13.6	13.8	14.2	15.0	14.0
Ba	67	68	78	88	68	82		68	86	85	90	78
Ce	13.3	14.3	15.1	15.8	10.7	14.4		12.7	14.5	15.4	15.0	14.1
Cl (ppm)	798	799	817	830	810	780	870	792	794	797	780	806
Dy	2.4	2.4	3.0	3.2		2.3		2.4	3.3	2.6	1.8	2.6
Er	1.7	1.7	1.0	1.2	2.6	1.3		1.2	1.1	1.9	1.8	1.5
Eu	0.9	0.9	0.8	1.2	0.5	0.9		0.8	0.6	0.9	1.0	0.8
Gd	2.5	3.0	2.6	3.5	3.4	2.6		2.0	2.9	2.1	2.3	2.7
Hf	1.6	1.5	1.6	1.2		1.2		1.5	3.0	3.3	1.7	1.8
La	4.4	4.4	4.3	5.2	4.2	5.1		4.0	4.7	5.2	5.0	4.6
Nb	0.9	0.9	1.0	0.8	1.2	1.0		1.0	1.0	1.5	1.2	1.0
Nd	9.4	9.3	9.8	13.7	4.7	9.5		9.3	9.2	9.2	9.4	9.3
Pb	2.5	1.7	2.0	2.9	3.2	1.6		1.9	3.1	3.2	2.6	2.5
Pr	2.5	2.2	2.1	2.3	1.6	1.9		1.9	2.2	2.1	2.4	2.1
Rb	3.1	1.9	3.6	3.2	2.4	3.2		2.3	4.2	4.3	4.0	3.2
S (ppm)	1270	1280	1380	1380	1370	1470	1460	1140	1420	1500	1040	1340
Sc	27.8	26.8	28.7	28.1	74.3	25.7		20.6	35.5	36.6	25.9	33.0
Sm	2.2	2.1	2.7	3.3		1.5		1.4	0.4	3.0	2.3	2.1
Sr	467	462	457	456	393	477		463	466	472	438	455
Ta	0.0	0.1		0.2	0.3	0.0				0.2		0.1
Th	0.6	0.6	0.6	0.6		0.5		0.3	0.9	0.5	0.5	0.6
U	0.1		0.2	0.2		0.1		0.2	0.2	0.2	0.2	0.2
V	182	189	216	200	231	192		184	214	219	181	201
Y	14.2	15.6	13.7	15.5	12.3	12.4		13.2	18.1	15.7	14.6	14.5
Yb	1.5	2.1	1.2	1.4	3.9	1.4		1.7	2.7	2.1	1.6	1.9
Zr	65	66	64	68	65	58		64	71	75	64	67

Table 3 (continued): Compositions corrected to equilibrium with mantle (Fo_{90}) and normalized to 100

Sample	IP 001	IP 003_1	IP 005	IP 016	IP 020	IP-Avg
SiO_2	48.51	47.67	51.44	48.24	48.31	48.83
TiO_2	1.23	1.39	1.86	1.31	1.27	1.41
Al_2O_3	15.59	15.89	13.95	15.72	15.67	15.36
FeO	6.09	6.02	5.95	6.00	6.05	6.02
Fe_2O_3	1.42	1.43	1.37	1.36	1.43	1.40
MnO	0.10	0.09	0.10	0.10	0.09	0.10
MgO	10.67	10.54	10.43	10.52	10.61	10.56
CaO	9.41	9.44	7.15	9.49	9.76	9.05
Na_2O	3.80	4.13	3.55	3.98	3.67	3.82
K_2O	0.74	0.88	1.54	0.80	0.71	0.93
P_2O_5	0.47	0.54	0.69	0.50	0.47	0.53
H_2O	1.91	1.91	1.91	1.91	1.91	1.91
%Ol add	6.5	5.5	6.9	7.7	5.9	6.5
Ba		393		318		356
Ce		64.6		45.1		54.8
Cl (ppm)	417	492	662	413	393	475
Dy		2.9		2.8		2.9
Er		1.2		2.5		1.8
Eu		1.8		1.8		1.8
Gd		3.8		3.7		3.7
Hf		2.4		2.3		2.4
La		22.0		19.2		20.6
Nb		7.3		5.7		6.5
Nd		28.6		22.4		25.5
Pb		4.8		3.9		4.4
Pr		7.3		5.7		6.5
Rb		8.7		6.8		7.8
S (ppm)	2560	2470	80	2200	2870	2030
Sc		23.6		23.3		23.5
Sm		4.9		4.9		4.9
Sr		1220		1100		1160
Ta		0.4		0.3		0.3
Th		2.7		1.8		2.3
U		0.9		0.6		0.7
V		217		181		199
Y		13.6		15.2		14.4
Yb		0.8		1.1		1.0
Zr		120		108		114

Appendix A: Uncorrected Major and Trace Element Data

Whitechuck LKT

Sample	WC 002_1	WC 002_2	WC 003	WC 007	WC_008	WC 013	WC 014	WC 017	WC 020_1	WC 020_2	WC 023
SiO_2	49.02	48.68	48.81	50.01	48.42	48.52	49.79	48.55	49.30	48.69	48.98
TiO_2	1.12	1.08	1.11	1.30	1.07	1.13	1.14	1.11	1.17	1.16	1.13
Al_2O_3	17.97	17.98	18.84	18.88	17.65	18.70	18.54	17.80	18.50	19.53	17.93
FeO^T	7.76	7.82	7.75	7.30	7.71	7.59	7.46	7.57	7.36	6.56	8.64
MnO	0.14	0.14	0.13	0.14	0.13	0.13	0.14	0.14	0.13	0.13	0.16
MgO	6.34	6.43	6.22	3.83	5.67	5.18	4.83	6.55	5.22	3.74	5.59
CaO	9.98	9.91	10.34	10.56	10.35	10.41	10.25	9.99	10.43	10.52	10.20
Na_2O	3.31	3.30	3.43	3.54	3.36	3.41	3.77	3.34	3.36	3.76	3.92
K_2O	0.38	0.39	0.43	0.47	0.42	0.43	0.44	0.39	0.42	0.46	0.47
P_2O_5	0.21	0.20	0.21	0.23	0.21	0.21	0.21	0.19	0.21	0.24	0.22
S	0.15	0.15	0.16	0.16	0.16	0.17	0.17	0.13	0.17	0.18	0.12
Cl	0.09	0.09	0.10	0.10	0.10	0.09	0.11	0.09	0.10	0.10	0.10
H_2O^c	1.5	1.8	0.5	2.1	2.0	1.2	0.6	1.9	1.3	0.9	1.2
CO_2^c	620	820	330	680	770	250	290	510	450	170	570
Total	96.46	96.20	97.57	96.55	95.25	96.04	96.91	95.90	96.37	95.11	97.54

Indian Pass CAB *Schreiber's Meadow CAB*

Sample	IP 001	IP 003_1	IP 005	IP 016	IP 020	SM 001	SM 005	SM 007	SM 025	SM 027	SM 029	SM 030	SM 032
SiO_2	47.94	47.66	52.77	47.59	48.10	52.60	51.03	51.54	47.59	48.58	51.14	57.11	50.65
TiO_2	1.35	1.54	2.14	1.41	1.42	1.32	1.34	1.27	0.68	1.22	1.78	1.94	1.16
Al_2O_3	17.09	17.61	16.06	16.87	17.51	18.42	19.63	18.48	18.83	17.23	16.22	17.24	17.76
FeO^T	6.40	6.13	6.69	6.92	6.26	7.55	5.31	6.07	9.69	8.29	8.70	6.18	6.33
MnO	0.11	0.10	0.12	0.11	0.10	0.16	0.10	0.12	0.18	0.16	0.17	0.12	0.12
MgO	5.61	5.86	4.26	6.16	5.07	2.63	3.10	3.65	4.14	4.79	4.36	3.07	5.34
CaO	10.32	10.47	8.23	10.19	10.90	9.77	10.49	10.34	11.32	9.35	7.55	5.82	9.77
Na_2O	4.17	4.58	4.08	4.27	4.10	4.63	4.33	4.27	2.48	4.15	4.90	5.20	3.54
K_2O	0.81	0.98	1.77	0.85	0.79	0.37	0.81	0.78	0.40	0.73	1.32	2.12	0.78
P_2O_5	0.51	0.60	0.80	0.53	0.52	0.21	0.43	0.39	0.16	0.30	0.51	0.70	0.36
S^a	0.30	0.29	0.01	0.26	0.33	0.10	0.16	0.16	0.07	0.15	0.12	0.02	0.15
Cl	0.05	0.05	0.08	0.05	0.04	0.02	0.05	0.05	0.02	0.05	0.04	0.05	0.05
H_2O^b	2.2	1.5	2.9	1.6	1.8	1.0	2.4	1.4	2.2	1.9	1.4	0.8	1.7
CO_2^b	1380	310	b.d.	970	1000	180	940	360	290	640	360	b.d.	420
Total	94.74	100.00	97.15	95.32	100.00	100.00	96.85	97.22	95.62	95.03	96.88	99.65	96.03

Major elements in wt. %, CO_2 in ppm. Unless otherwise noted, analyses performed at University of Oregon CAMCOR lab. Fe reported as total FeO^T [a]Analysis performed at Washington State University [b]Performed with FTIR at University of Oregon.

Appendix A (continued): Uncorrected Major and Trace Element Data

Whitechuck LKT

Sample	WC_002	WC_002_2	WC_003	WC_007	WC_008	WC_013	WC_017	WC_020_1	WC_020_2	WC_023
Ba	77	79	91	108	81	98	79	104	107	110
Ce	15	17	18	19	13	17	15	17	20	18
Dy	2.8	2.8	3.5	3.9	-	2.7	2.8	4.0	3.2	-
Er	2.0	1.9	1.1	1.4	3.1	1.5	1.4	1.3	2.4	2.2
Eu	1.0	1.0	0.9	1.5	-	1.1	0.9	0.7	1.2	1.2
Gd	2.9	3.4	3.0	4.3	-	3.1	2.3	3.5	2.7	2.8
Hf	1.9	1.7	1.8	1.5	-	1.4	1.7	3.6	4.2	2.0
La	5.1	5.1	5.0	6.3	-	6.1	4.6	5.6	6.6	6.1
Nb	1.1	1.0	1.1	1.0	-	1.2	1.1	1.2	1.9	1.5
Nd	11	11	11	17	6	11	11	11	12	11.4
Pb	2.9	2.0	2.4	3.5	3.8	1.9	2.2	3.8	4.1	3.2
Pr	2.9	2.5	2.5	2.8	1.9	2.3	2.2	2.6	2.6	2.9
Rb	3.6	2.2	4.2	3.9	-	3.9	2.6	5.1	5.4	4.9
Sc	31	30	33	33	85	30	23	42	44	30
Sm	2.6	2.5	3.2	4.0	-	-	-	-	3.7	2.8
Sr	542	535	534	559	465	574	536	561	596	532
Ta	-	0.1	-	-	-	-	-	-	0.2	-
Th	0.7	0.6	0.7	0.8	-	0.6	-	1.0	0.7	0.7
U	0.1	-	0.2	0.3	-	0.2	0.2	0.3	0.2	0.2
V	209	217	251	243	270	229	212	255	273	218
Y	16	18	16	19	15	15	15	22	20	18
Yb	1.7	2.4	1.4	1.6	-	1.6	1.9	3.2	2.6	1.9
Zr	75	76	75	84	77	70	74	86	95	78

Indian Pass CAB		*Schreiber's Meadow CAB*				
Sample	IP_016	IP_003_1	SM_025	SM_027	SM_029	SM_030	SM_032
Ba	346	432	211	265	387	554	251
Ce	49	71	13	22	45	59	27
Dy	3.1	3.1	2.2	1.8	7.6	5.7	1.5
Er	2.7	1.3	0.8	-	4.0	4.3	2.0
Eu	1.9	2.0	-	1.1	2.3	1.6	0.9
Gd	4.0	4.2	-	4.8	6.0	5.3	1.7
Hf	2.5	2.7	1.2	-	4.7	5.0	2.8
La	21	24	4	9	20	24	11
Nb	6.2	8.0	1.5	3.4	9.2	12.8	5.5
Nd	24	31	9	13	25	31	16
Pb	4.3	5.2	2.5	1.3	5.1	7.8	2.9
Pr	6.2	8.0	1.0	1.6	6.7	7.3	2.7
Rb	7	10	7	5	16	41	5
Sc	25	26	30	33	32	20	27
Sm	5.3	5.3	1.7	2.1	7.2	5.6	2.8
Sr	1200	1340	790	520	480	390	530
Ta	0.3	0.5	-	2.0	0.5	1.1	-
Th	2.0	3.0	-	-	2.4	5.1	-
U	0.6	0.9	0.3	-	1.0	1.4	-
V	197	237	120	259	201	223	225
Y	17	15	9	20	36	35	17
Yb	1.2	0.9	1.2	2.3	1.8	2.0	-
Zr	117	132	38	102	256	274	108

All trace elements in ppm. Analyses performed with LA-ICP-MS at Oregon State University

Appendix B: Extended Methods

Sample Preparation

Tephra samples were collected from as far down within the cinder cone deposits as possible, though not quite at the basal layer. Tephra size was limited to ≤ 1 cm, though most sample sets were smaller (3mm-0.1mm) for ease of separation. Sample sets were dried and sieved, to isolate tephra between 0.25 and 1.25 mm. Olivine and other dense minerals were isolated from matrix using heavy-liquid density separation techniques (lithium tetrabromoethane).

Once separated, olivine crystals were inspected under binocular light microscope and refractive index oil (refractive index of 1.65) to determine those most likely to contain appropriate melt inclusions. Inclusions appropriate to this study were primary inclusions (round or oval-shaped and not associated with olivine cracks), glassy (no evidence of secondary mineral growth), and larger than 50 microns. These inclusions were typically very light brown, completely transparent, and often contained a clearly visible shrinkage bubble.

Olivine crystals were individually mounted on round, 1 in diameter glass petrographic slides, using Crystalbond adhesive (a common thermoplastic mounting matrix) melted onto each slide on a hotplate. The smallest possible amount of Crystalbond was used that left enough surface area outside of the crystal to maintain a flat polishing surface. Too little Crystalbond would leave the crystal sitting above the thermoplastic where it would become rounded.

Once the crystals were mounted, each one was lightly polished using 600 grit wet/dry sandpaper (used in automobile detailing). After this initial polish (3-4 passes), the crystal was inspected under light microscope (with a small drop of refractive index oil, if necessary) to establish the location and approximate depth of a good inclusion. Once identified, the olivine hosts were slowly polished by hand with 600 grit sandpaper until each inclusion was intersected. Intersected surfaces showed up as small, inner clear areas within inclusions as the light was turned down to its lowest level. Many inclusions were lost while gaining the experience to see this intersection.

Mounted crystals were then washed carefully in cold water (warm water may soften the thermoplastic) using dishwashing soap, to remove any embedded grit. This was important to avoid cross-contaminating the lap wheel with different grit sizes. Each crystal was polished for 3-5 minutes on a lap wheel with 6-micron diamond paste. Small amounts of olive oil (3-6 drops) were used to lubricate the wheel and to avoid removing the crystal from the thermoplastic accidently. While polishing a large set of inclusions, frequent observation under reflected light was done to make sure enough polishing compound remained on the cloth and that no cross-contamination of grit sizes from the previous step had occurred (noted by grooves within the crystal or the thermoplastic). Once polished, the mounted crystals were then washed again to remove any traces of the 6-micron paste and dried. Mounted crystals were then polished with 1-micron diamond paste for 1-3 minutes, inspecting them frequently under reflected light.

Mounted and polished crystals were then heated on a hotplate situated beneath a light microscope until the thermoplastic melted slightly. Using tweezers, each crystal was

flipped onto the polished side and pressed down gently to ensure that there was little thermoplastic beneath the crystal. This step was vital; calculation of the inclusion composition is dependent upon the wafer thickness, measured initially on the mounted host. After flipping, each inclusion was intersected from the other side of the crystal, using 600 grit sandpaper, then 6-micron and 1-micron paste. Olivine host crystals were easiest to deal with (and not break) in further steps if they were polished no thinner than 60 microns, and preferably closer to 100 microns. Very small, or thin, inclusions were not totally intersected on this side, and the extra olivine was subtracted out mathematically post-analysis. This required, however, that when these particular host-crystals were mounted for microprobe analysis that the intersected side was positioned face up to remain exposed. Further polishing (and washing between steps) was carried out as before.

Doubly polished crystals were then photographed (as much of the total crystal as possible), with the photographs immediately printed out and stored in a binder. This allowed for easy identification during later analysis, especially for crystals with multiple inclusions.

Before removing olivine-hosts from their mounts, each crystal thickness was measured with a digital micrometer. Slide thickness was measured in three different spots, averaged, and subtracted from the thickness of the combined crystal and slide.

Preparation for FTIR, EPMA and LA-ICPMS analysis

Each olivine-host was removed from the Crystalbond thermoplastic by setting it upside down in a watchglass filled with acetone. After approximately 30 seconds the

crystals dropped from the slide into the watch-glass. Any remaining thermoplastic was dissolved from the crystal by refreshing with new acetone in at least three cycles of pipetting out and refilling. Once washed, the crystal was transferred to a slide holding a 13x2mm, round NaCl disc for FTIR analysis.

After analysis by FTIR, the crystals were mounted for microprobe analysis. Using double-sided tape mounted on a sheet of aluminum, locations were marked using a round 2.5 cm diameter, 1 cm thick plastic mount with 7 holes drilled into it by the machine shop at the University of Oregon. The mount was pressed down upon the tape, leaving an impression where each hole was located. Within each impression, between 1 and 5 crystals were placed (intersected side down, if not doubly intersected) on the tape. As each crystal was placed, its location was recorded on a map of the mount. Once all of the crystals were placed, the mount was set back over them.

Each hole in the mount was gently filled with a Cl-free epoxy and set aside to harden for 12 hours. After this initial hardening, the mount was placed in a 60°C oven for 24 hours to finish curing. After curing, the mount was removed and polished, using 15 micron, 6 micron and 1 micron diamond paste, with careful washing between each step. This mount was used for both EPMA and LA-ICPMS analysis.

Appendix C: Partition Coefficients

	Olivine partition coefficients	Lherzolite bulk partition coefficient (Workman & Hart, 2005)	Lherzolite bulk partition coefficient (Kelley et al. 2006)
Ba	0.0099	0.00012	0.00012
Ce	0.006	0.022	0.011
Cl	0.0013	0.003	0.003
CO_2	0		
Dy	0.013	0.079	0.06
Er	0.0256	0.097	0.08
Eu	0.0074	0.05	0.035
Gd	0.01	0.056	0.04
H_20	0.001	0.012	0.012
K_2O		0.003	0.003
Hf	0.013		
La	0.0067	0.01	0.0075
Nb	0.01	0.0034	0.003
Nd	0.0059	0.031	0.02
Pb	0.0001		
Pr	0.006		
Rb	0.0098		
S	0		
Sc	0.17		
Sm	0.0066	0.045	0.03
Sr	0.014	0.025	0.011
Ta	0.03		
Th	0.0001	0.001	0.0015
Ti	0.02	0.058	0.04
U	0.002	0.0011	0.0011
V	0.06		
Y	0.01	0.088	0.095
Yb	0.0491	0.115	0.095
Zr	0.012	0.033	0.03

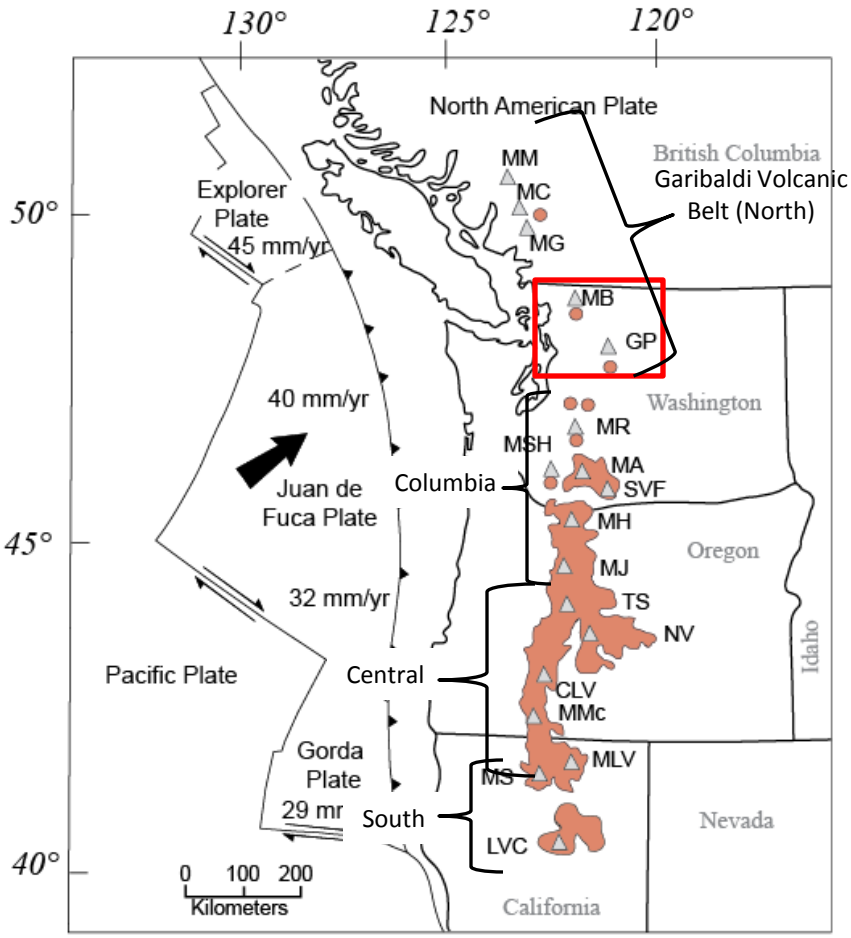

Figure 1: The Cascade arc. Orange regions denote wide-ranging mafic activity. Figure from DeBari et al. (submitted) modified from Borg et al. (1997). Segments are from Schmidt et al. (2008).

MM, Meager Mountain; MC, Mount Cayley; MG, Mount Garibaldi; MB, Mount Baker; GP, Glacier Peak; MR, Mount Rainier; MSH, Mount St. Helens; MA, Mount Adams; SVF, Simcoe Volcanic Field; MH, Mount Hood; MJ, Mount Jefferson; TS, Three Sisters; NV, Newberry Volcano; CLV, Crater Lake Volcano; MMc, Mount McLoughlin; MLV, Medicine Lake Volcano; MS, Mount Shasta; LVC, Lassen Volcanic Center

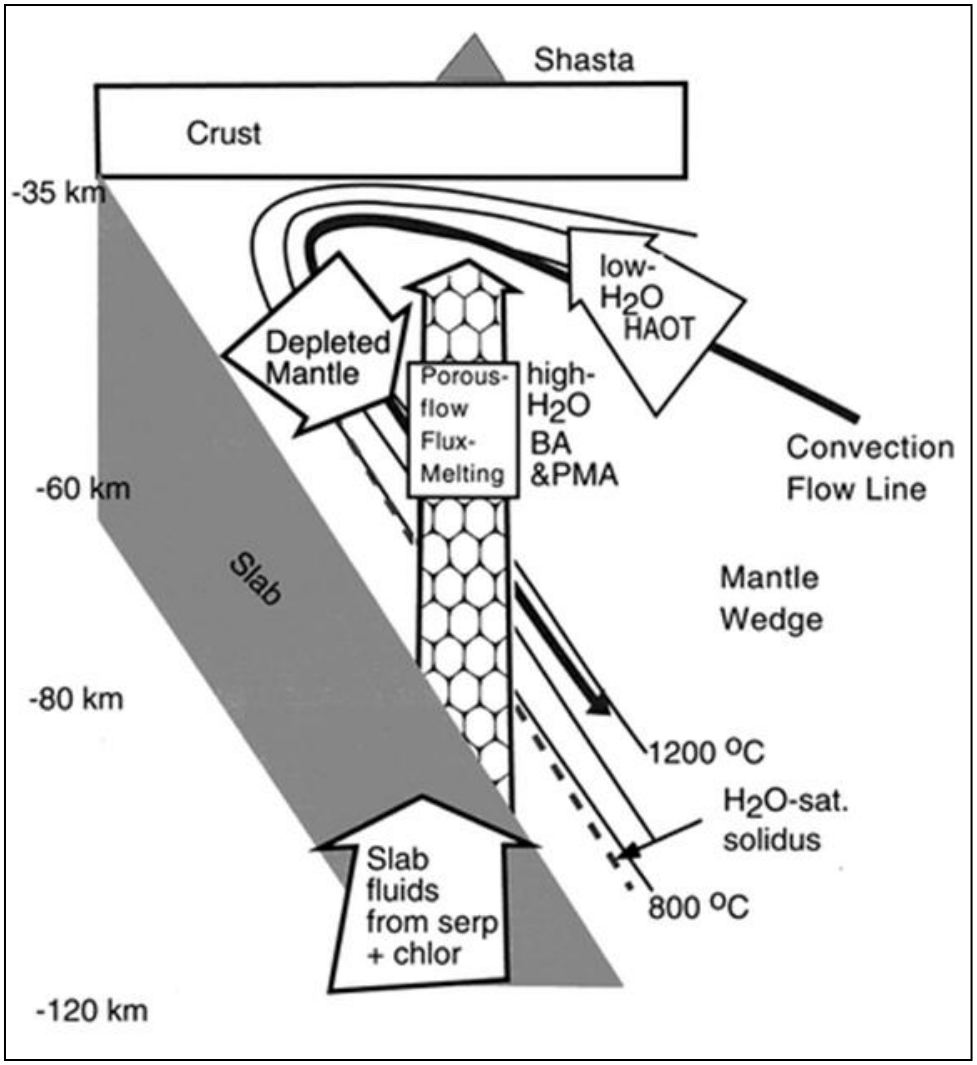

Figure 2: Grove et al. (2002), proposed this model of magma generation at Mount Shasta—accounting for low potassium tholeiite (LKT) magmas (called here HAOT—high alumina olivine tholeiite) through decompression melting in the mantle wedge and calc-alkaline basalt and basaltic-andesite (CAB) magmas (called here BA) and another sub-type (primitive magnesian andesite-PMA) through fluid-flux melting of a depleted mantle that is descending along the downgoing slab. Figure from (Grove et al., 2002).

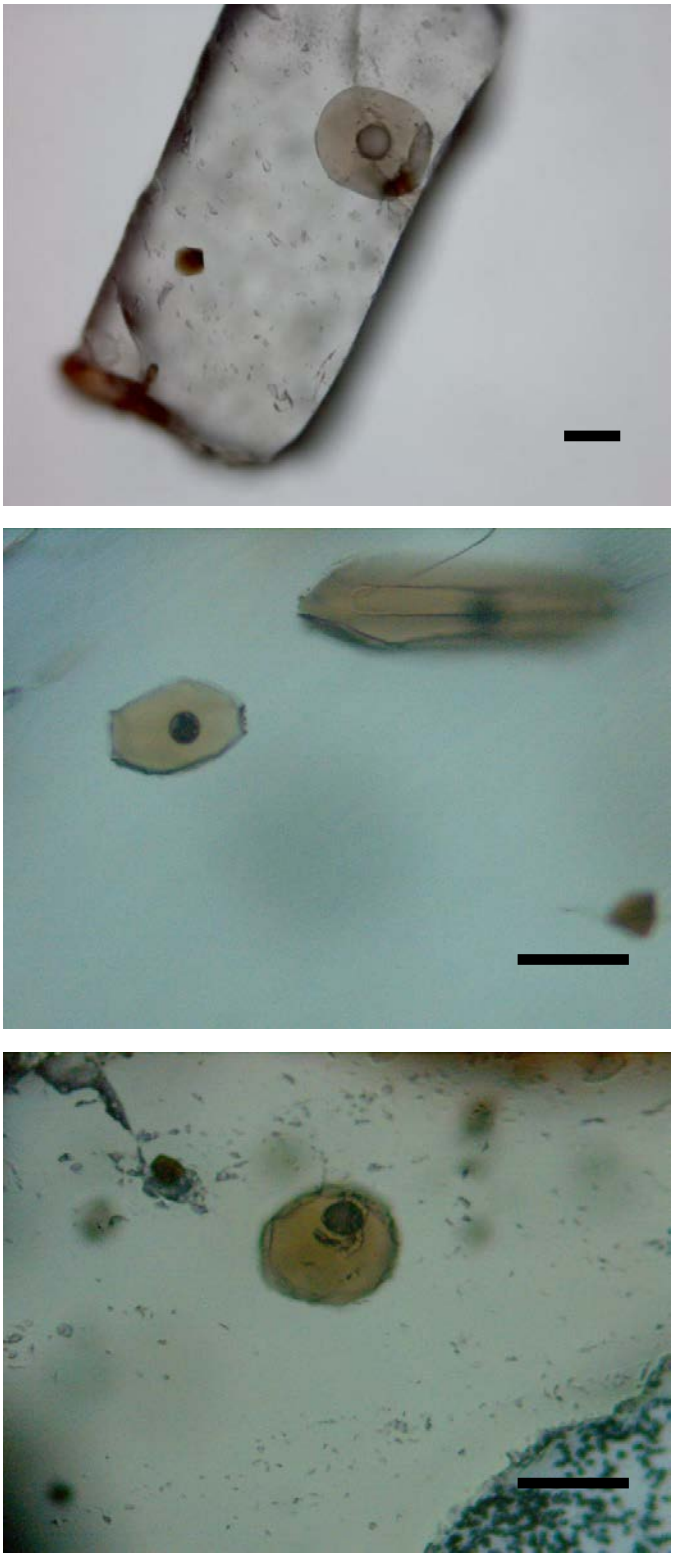

Figure 3: Typical melt inclusions used in this study. Inclusions are glassy, round or oval, and most contain a vapor bubble. Scale bars are 50 microns.

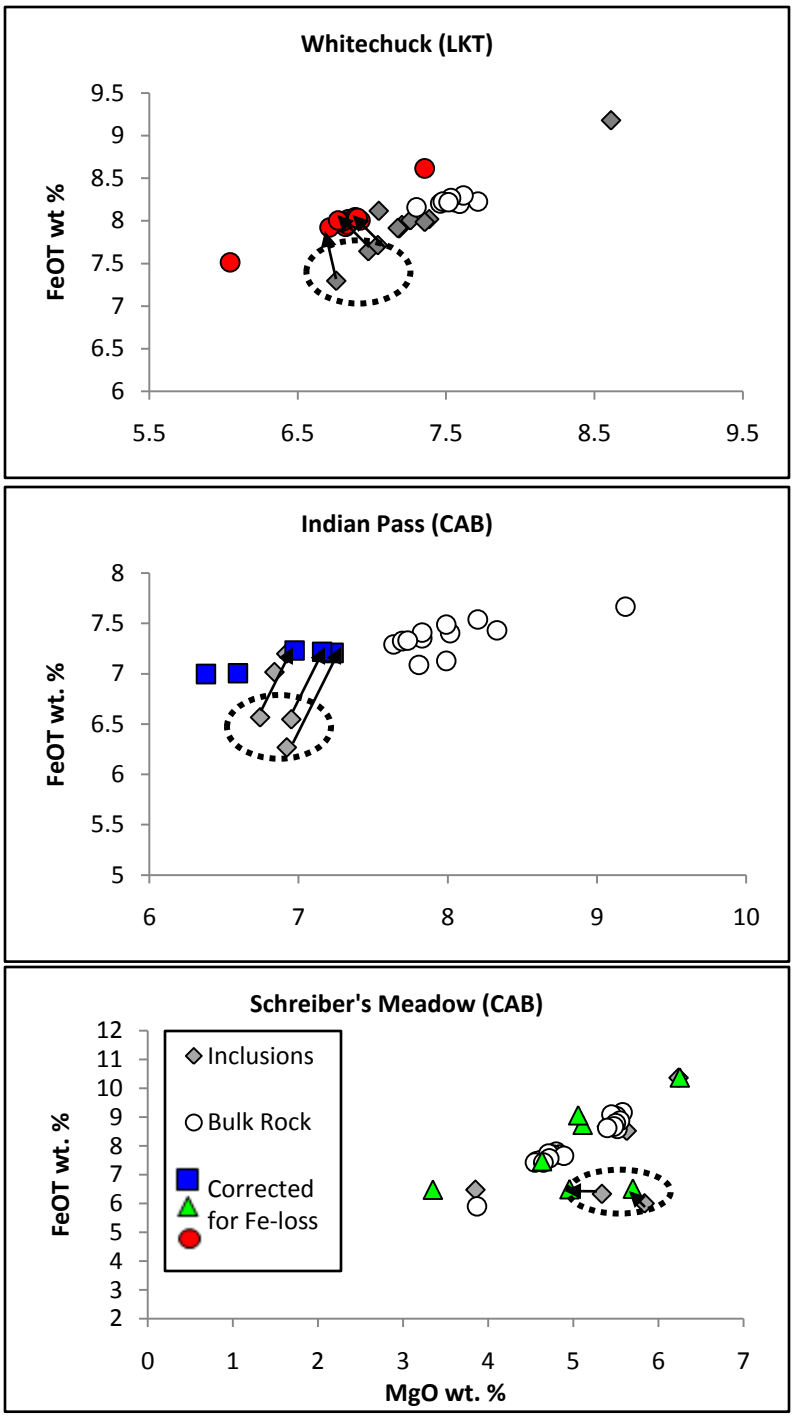

Figure 4 : Uncorrected inclusion data (grey diamonds) corrected, if necessary, for iron-loss (red, green and blue symbols). Circled inclusions (grey) are those that required this correction. Two inclusions from Schreiber's Meadow did not fall within the bounds of bulk rock compositions despite corrections (shown). Bulk rock data for Glacier Peak from DeBari et al., submitted. Bulk rock data for Mt. Baker from Moore and DeBari, submitted.

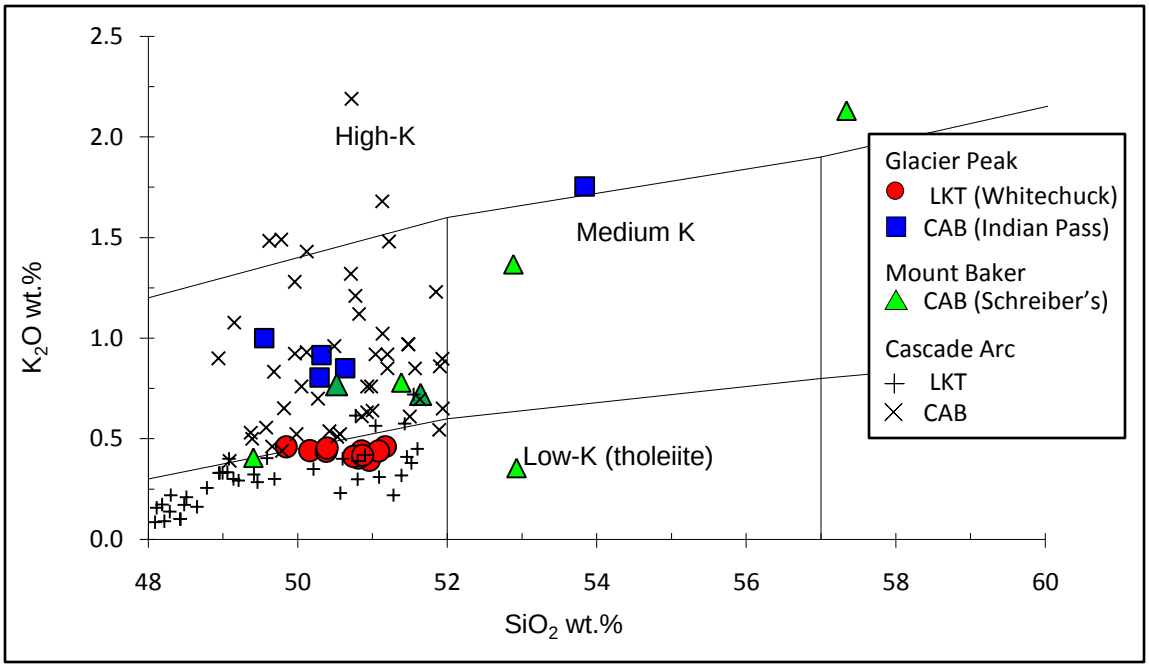

Figure 5 : K_2O vs. SiO_2 for corrected inclusion compositions (filled symbols) compared to Cascade arc primitive magmas. Arc LKTs and CABs are compiled from the GeoRoc database (Bacon, 1997; Conrey et al., 1997; Green and Sinha, 2005; Grove et al., 2002; Hildreth et al., 2003; Le Voyer et al., 2010; Leeman et al., 2005a; Rowe et al., 2009; Ruscitto et al., 2010; Sisson and Layne, 1993). Fields are from Gill (1981).

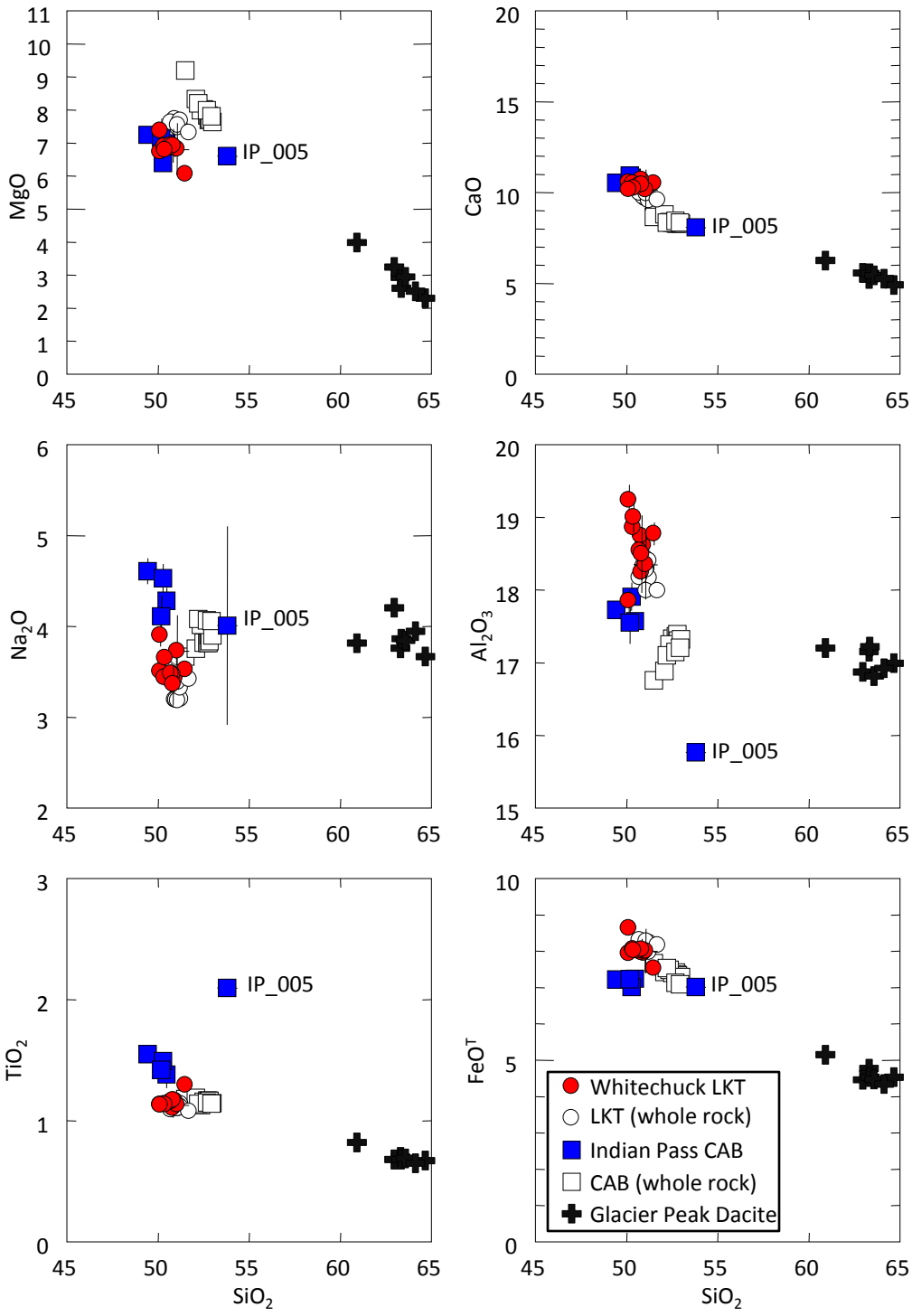

Figure 6: SiO_2 vs. major element for corrected Glacier Peak melt inclusions (red and blue symbols). Whole rock and dacite analyses of DeBari and et al. (submitted) shown for comparison. Inclusion IP_005 does not cluster with other compositions. Error bars are shown or are smaller than symbols. Oxides in wt. %.

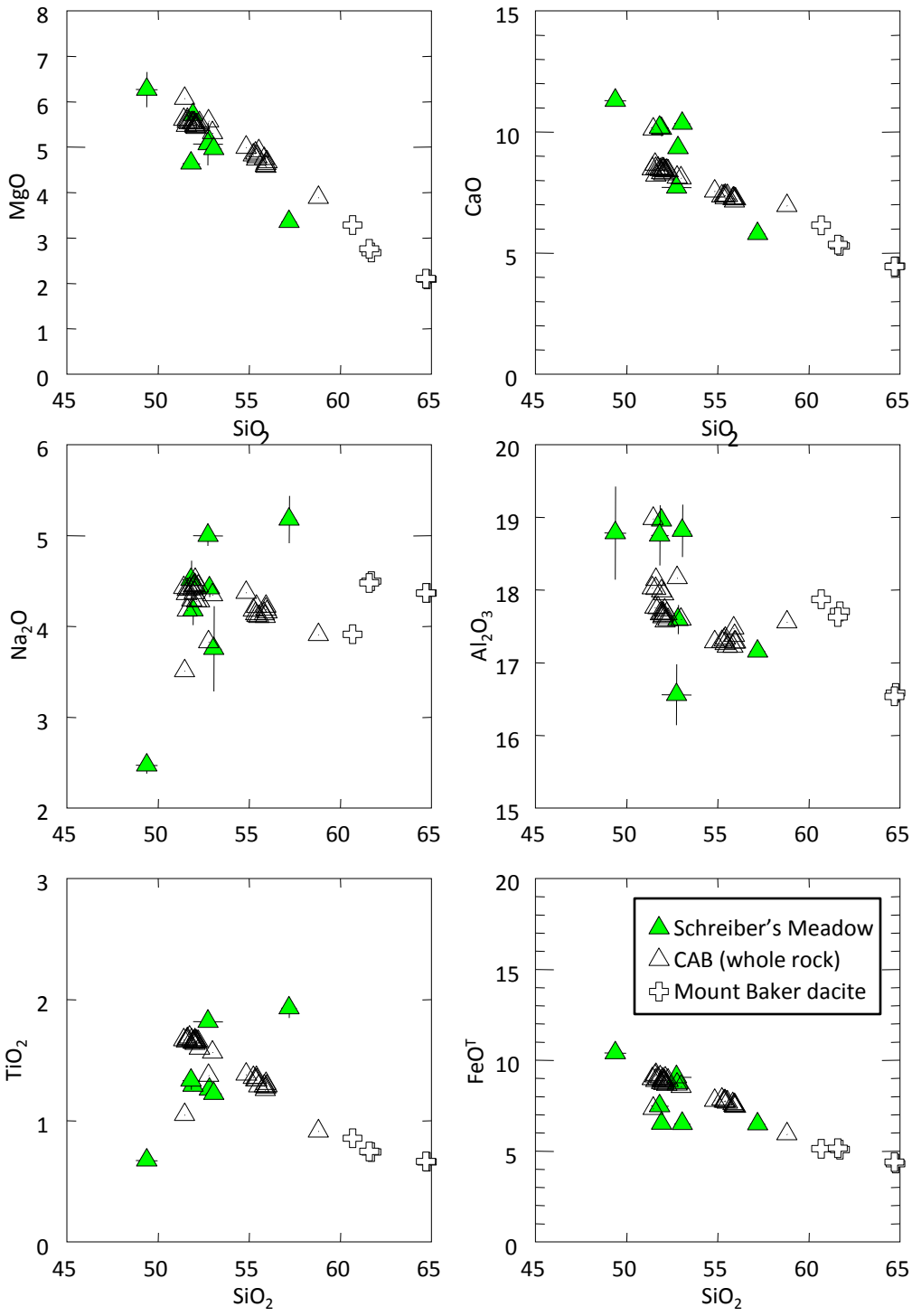

Figure 7: SiO_2 vs. major element for corrected Mt. Baker melt inclusions (green symbols). Associated Sulphur Creek lava flow (Green, 1988; Hildreth et al., 2003, Moore and DeBari, submitted) and dacite analyses (Baggerman and DeBari, in press) shown for comparison. Error bars are shown or are smaller than symbols. Oxides are in wt. %.

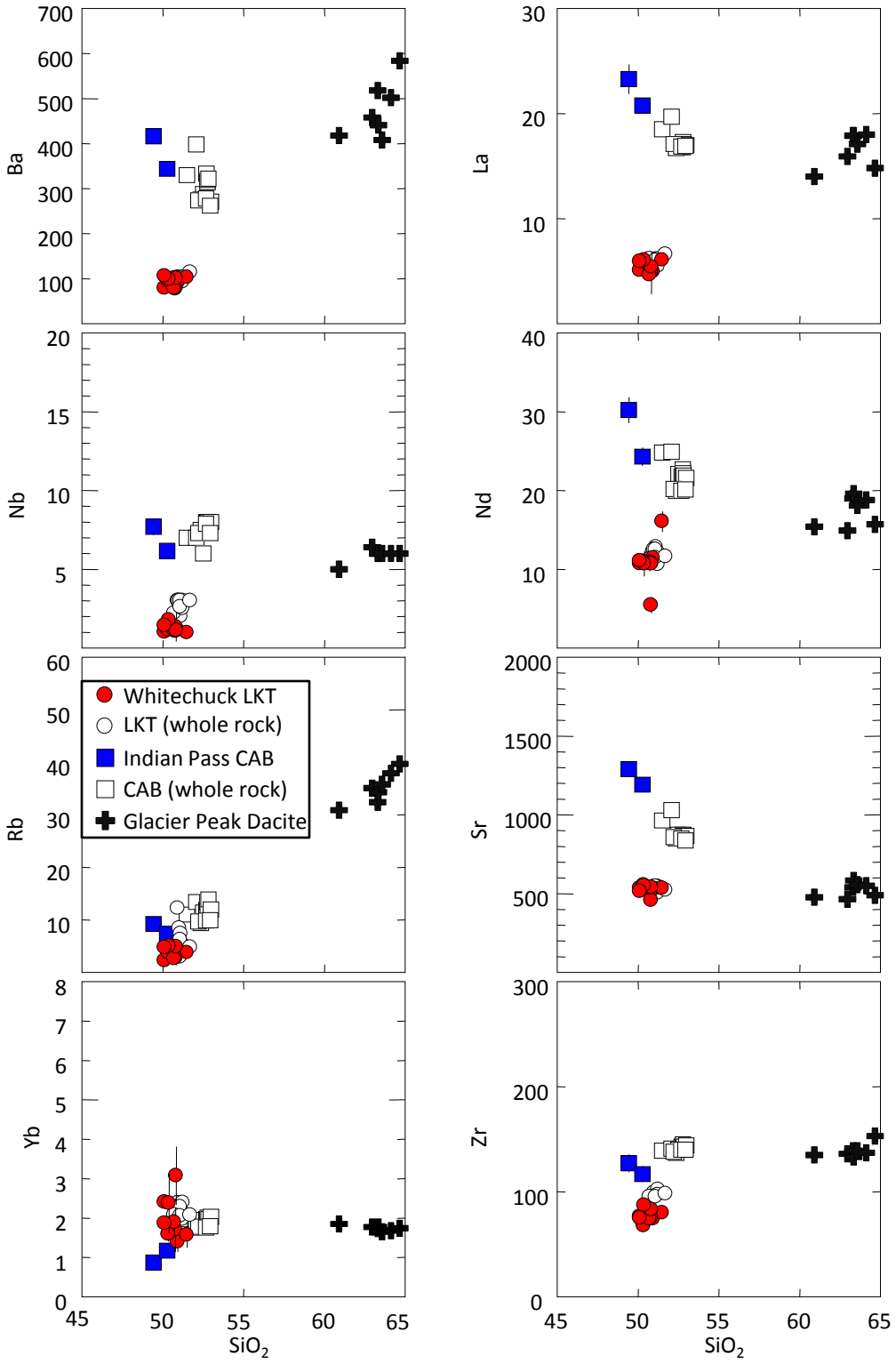

Figure 8: Trace element comparisons of Whitechuck (LKT) and Indian Pass (CAB) inclusion compositions with whole rock and dacite analyses of DeBari and Taylor (submitted) shown for comparison. Error bars are shown or are smaller than symbols.

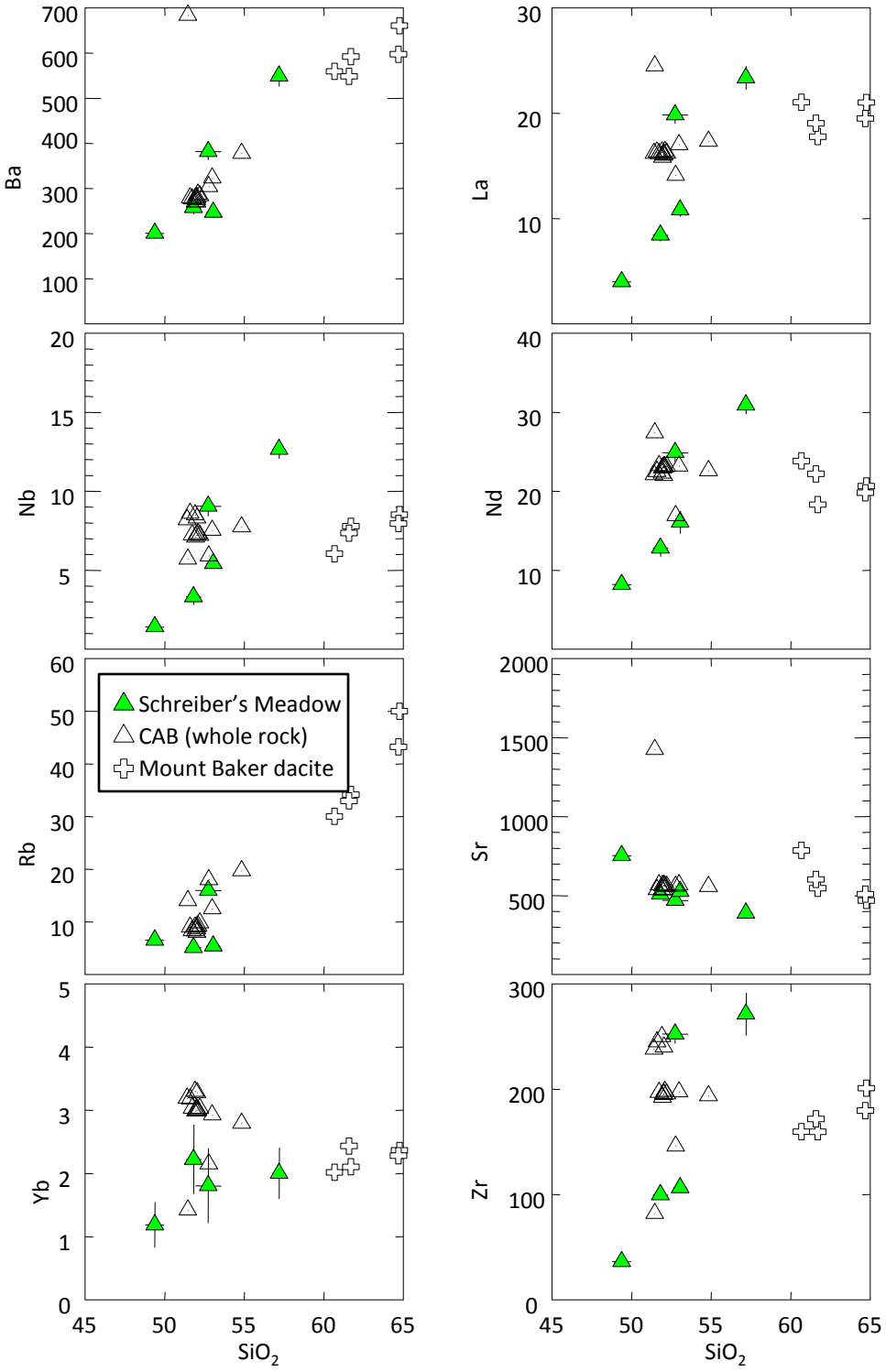

Figure 9: Trace element comparisons of Schreiber's Meadow (CAB) inclusion compositions with whole rock analyses from the associated Sulphur Creek lava flow (Green, 1988; Hildreth et al., 2003, Moore and DeBari, submitted) and dacite analyses (Baggerman and DeBari, in press) shown for comparison. Error bars are shown or are smaller than symbols.

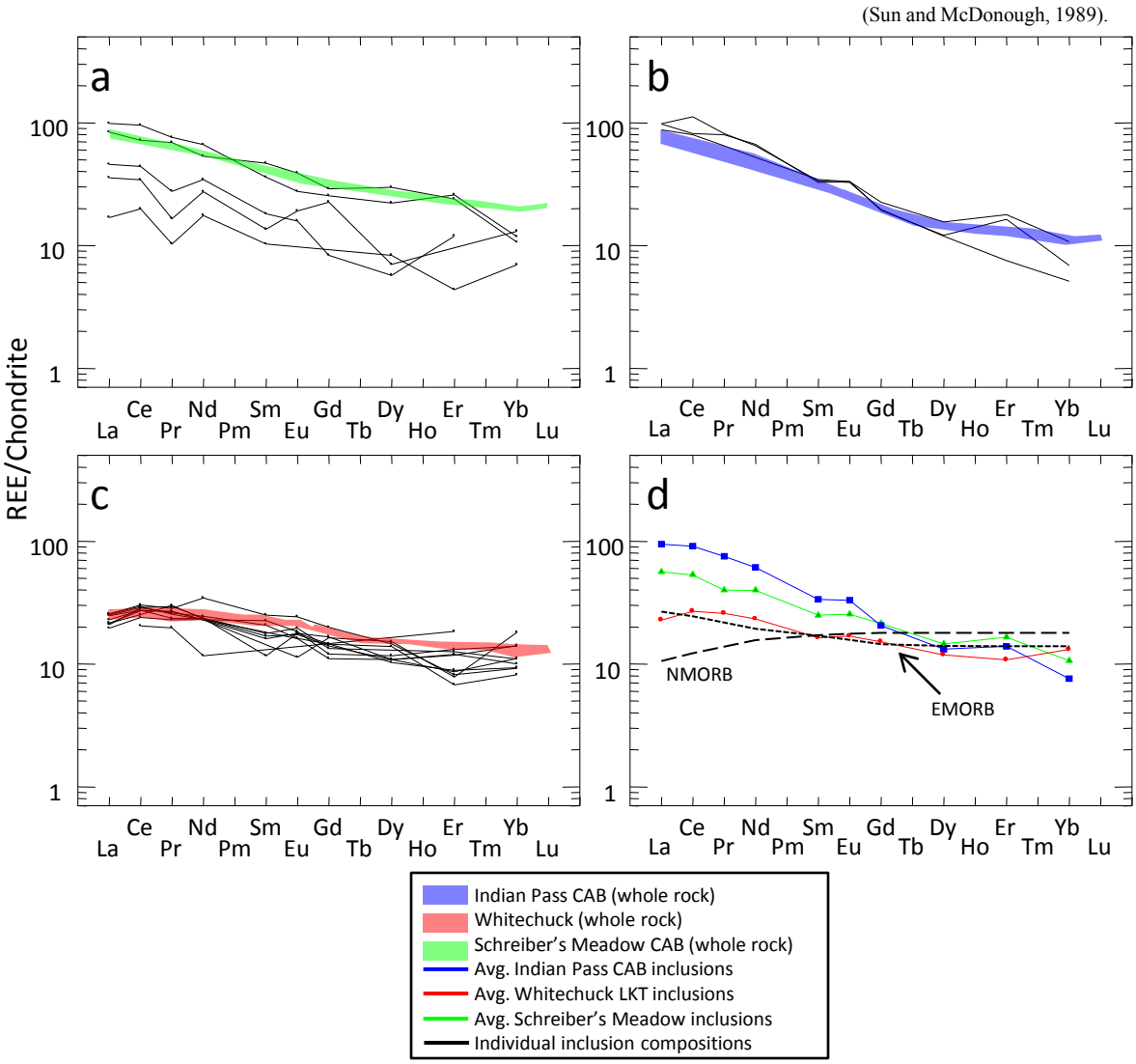

Figure 10: Chondrite-normalized rare earth element patterns for melt inclusions . (a) Schreiber's Meadow melt inclusions and field showing range of associated lava flow whole rock compositions. (b) Indian Pass CAB melt inclusions and whole rock field. (c) Whitechuck melt inclusions and whole rock field. (d) Comparison of average melt inclusion compositions with NMORB and EMORB. Whole rock data from DeBari et al. (submitted) [Glacier Peak] and Moore and DeBari (submitted) [Mount Baker]. EMORB and NMORB compositions from Sun and McDonough (1989).

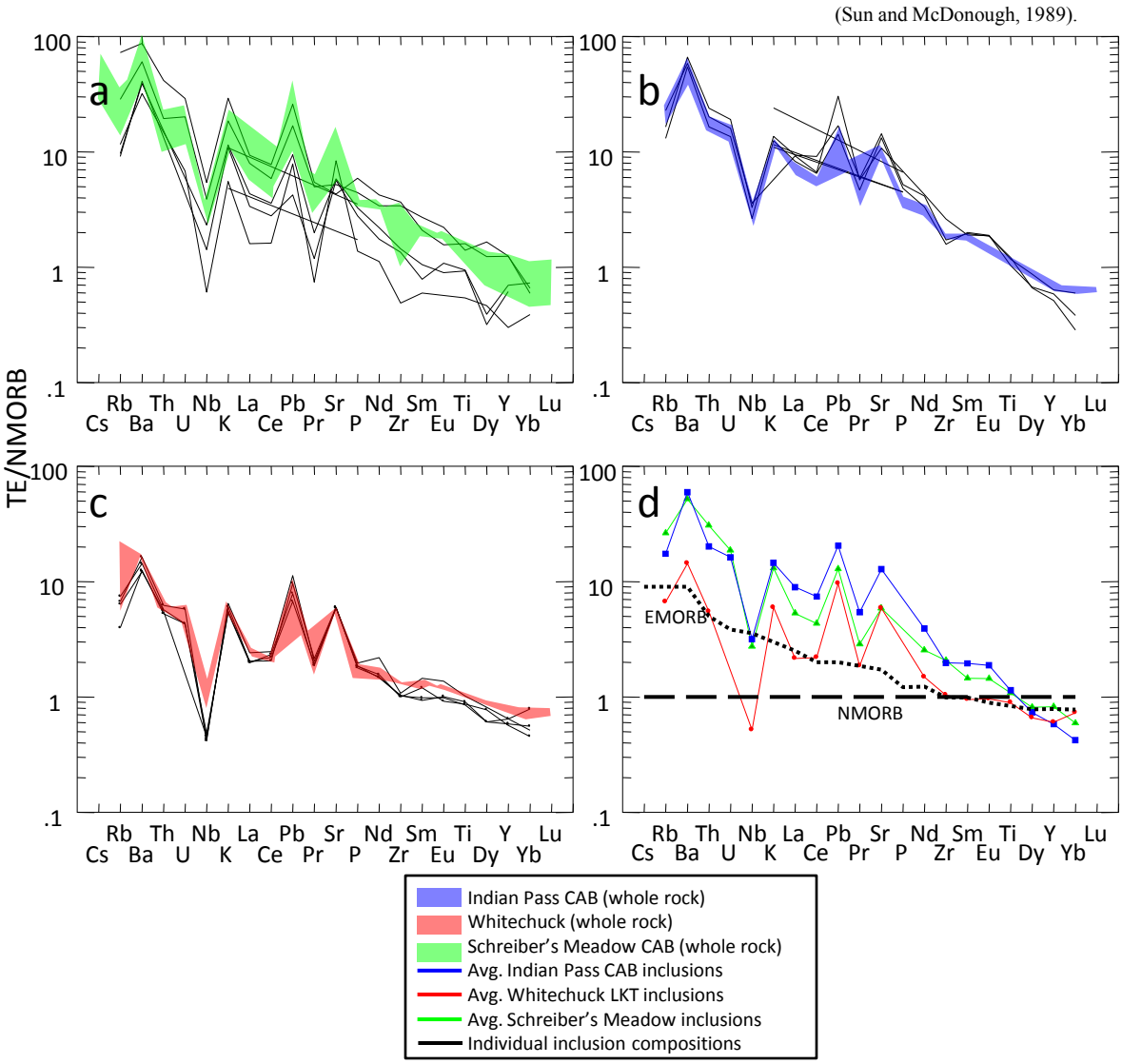

Figure 11: NMORB-normalized trace element patterns for corrected melt inclusions. (a) Schreiber's Meadow melt inclusions and field showing range of associated lava flow whole rock compositions. (b) Indian Pass CAB melt inclusions and whole rock field. (c) Whitechuck melt inclusions and whole rock field. (d) Comparison of average melt inclusion compositions with NMORB and EMORB. Whole rock data from DeBari et al. (submitted) [Glacier Peak] and Moore and DeBari (submitted) [Mount Baker]. EMORB and NMORB compositions from Sun and McDonough (1989).

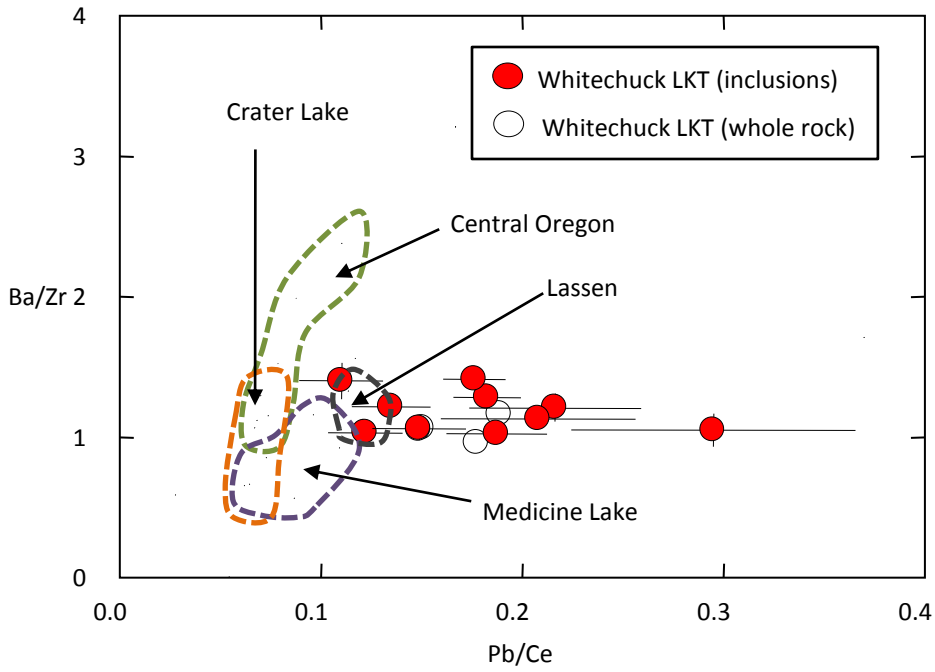

Figure 12: Common H_2O proxies (Ba/Zr and Pb/Ce) for corrected inclusions (filled symbols) and whole rock (open symbols). Fields for Cascade LKT shown for comparison. Data sources: Whitechuck whole rock (DeBari et al., submitted) Medicine Lake, Lassen and Crater Lake (Bacon, 1997), Central Oregon (Rowe et al., 2009).

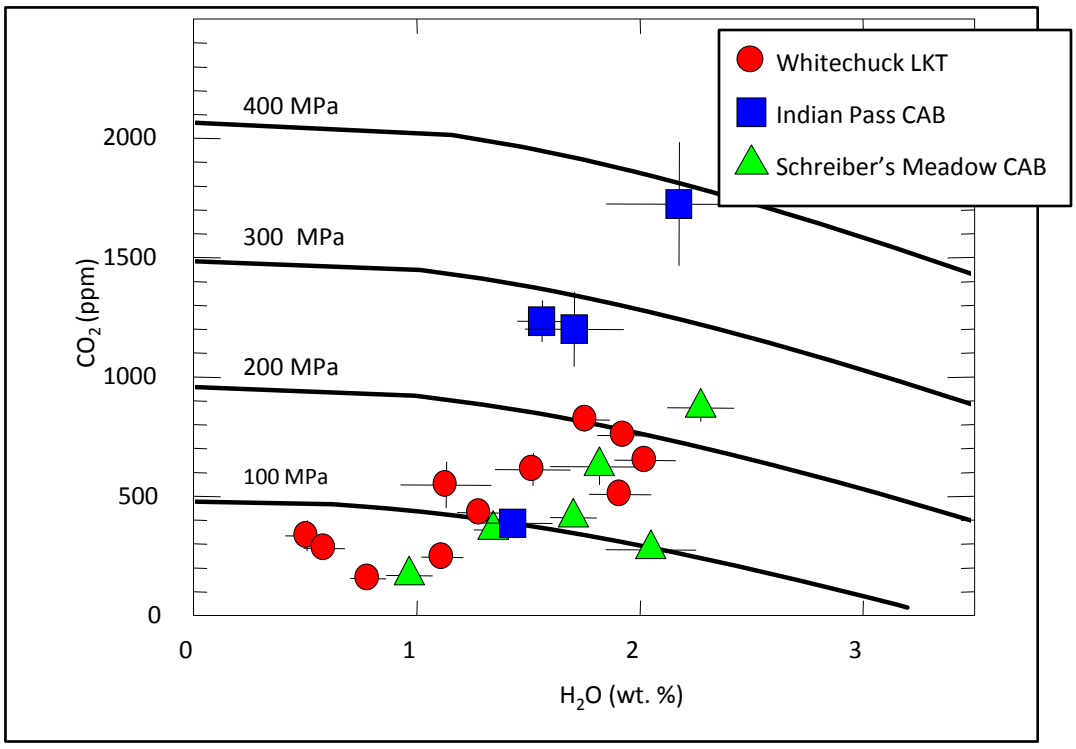

Figure 13: CO_2 vs. H_2O . Isobars showing minimum pressures at which inclusions were entrapped in crystallizing olivine hosts. Pressures calculated with VolatileCalc (Newman and Lowenstern, 2002). Error bars are shown or are smaller than symbols. Sample IP_005 (Glacier Peak CAB) is not shown, but has H_2O concentration of 1.05 wt. % and CO_2 concentrations below detection.

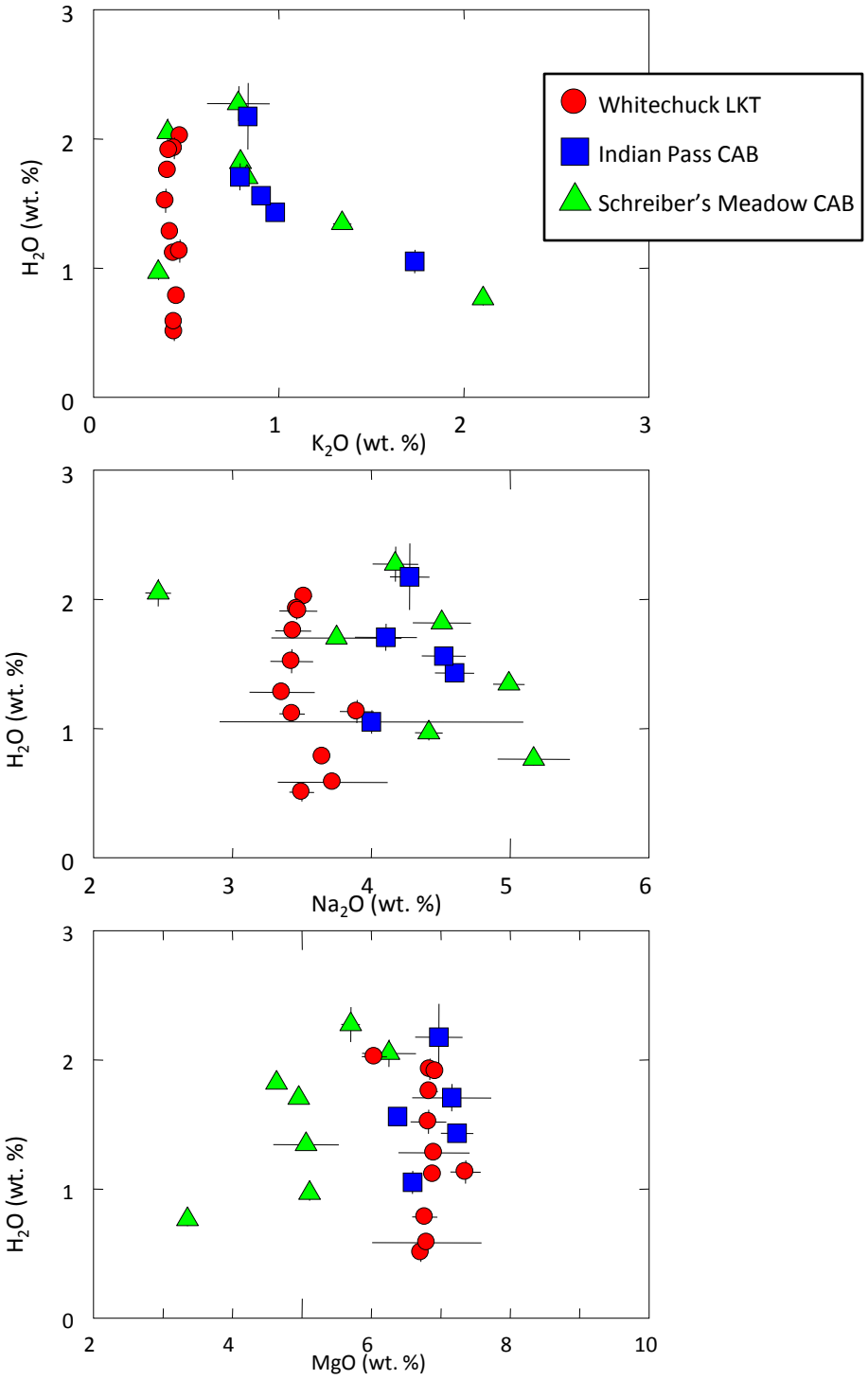

Figure 14: H_2O vs. alkalis and MgO. Error bars are shown or are smaller than symbols.

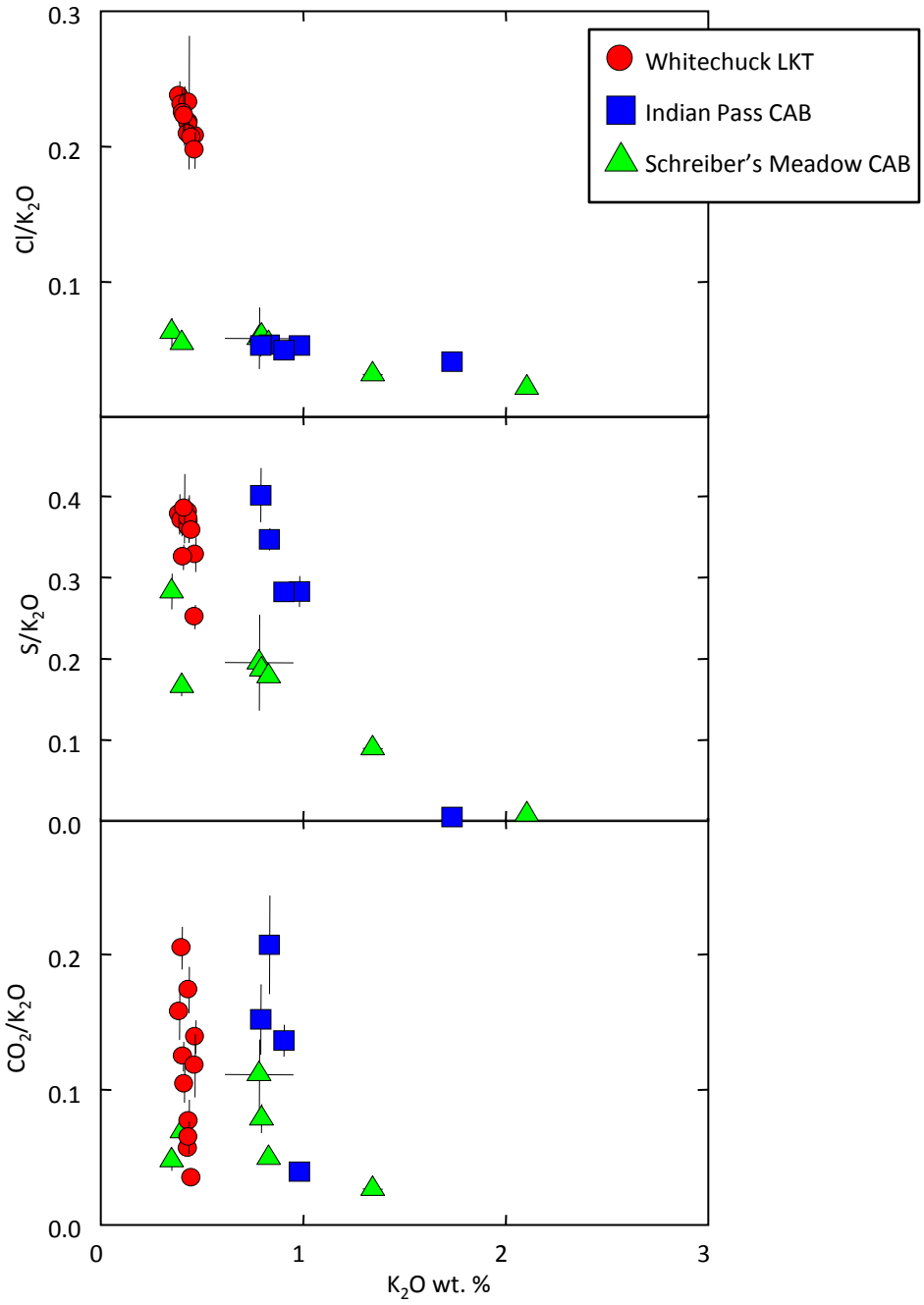

Figure 15: Volatiles vs. K_2O (using K_2O as a proxy for increasing fractionation) with corrected inclusion compositions. Volatiles for Whitechuck (red circles) have wide-ranging variability at similar degrees of fractionation, whereas Indian Pass and Schreiber's Meadow inclusions show decreasing volatile concentrations with increasing fractionation. Error bars are shown or are smaller than symbols.

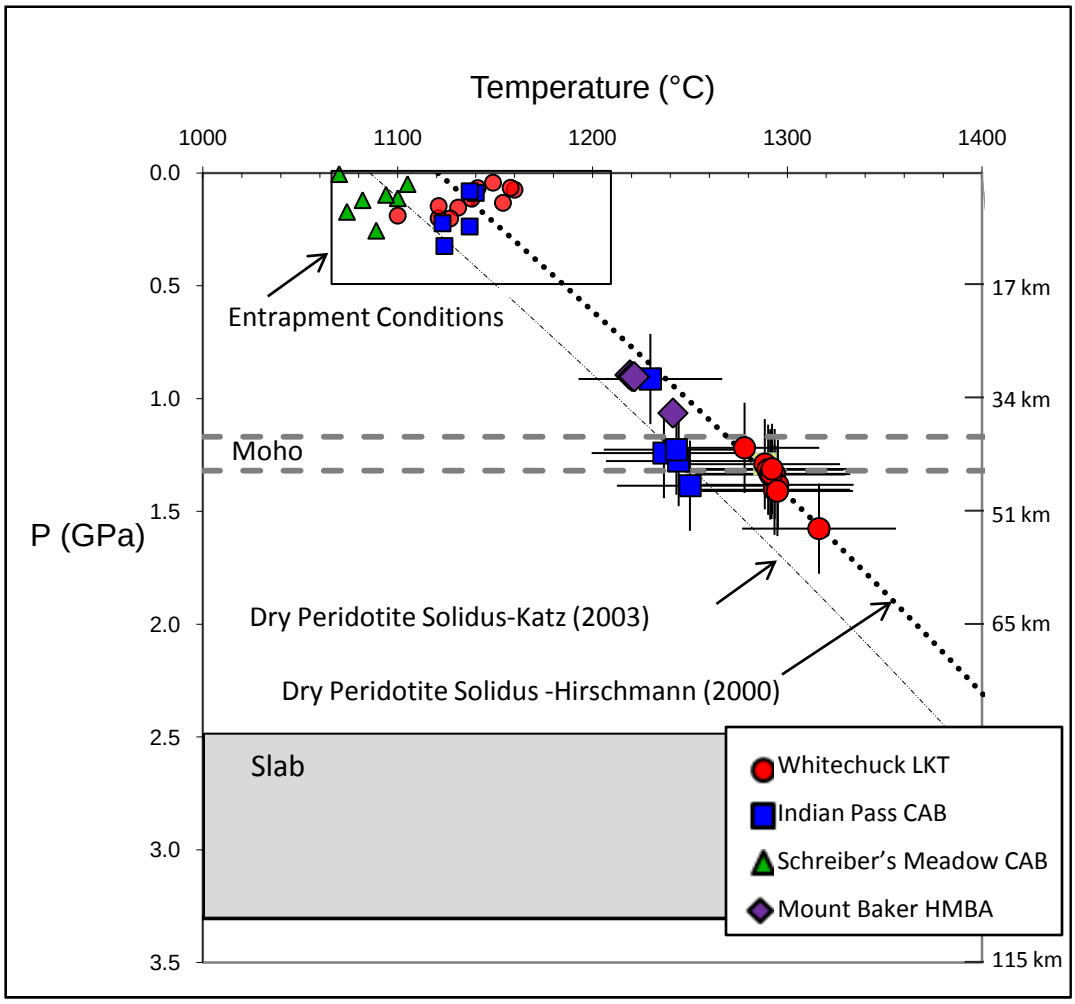

Figure 16: Pressure and temperature of last equilibration of melts with the mantle calculated with the geobarometer and geothermometer of Lee et al. (2009), using inclusion compositions corrected to mantle equilibrium. Entrapment pressures calculated with VolatileCalc (Newman and Lowenstern, 2002) , temperature calculated with Sugawara, 2000), both using inclusion compositions prior to correction to mantle values. For comparison, the High-Mg Basaltic Andesite (HMBA) Tarn Plateau primitive magma from Mount Baker (Moore and DeBari, submitted) is shown in purple. Slab depth is between 80-100 km (McCrory et al, 2004). Moho depth is between 40-45 km (Mooney and Weaver, 1989).

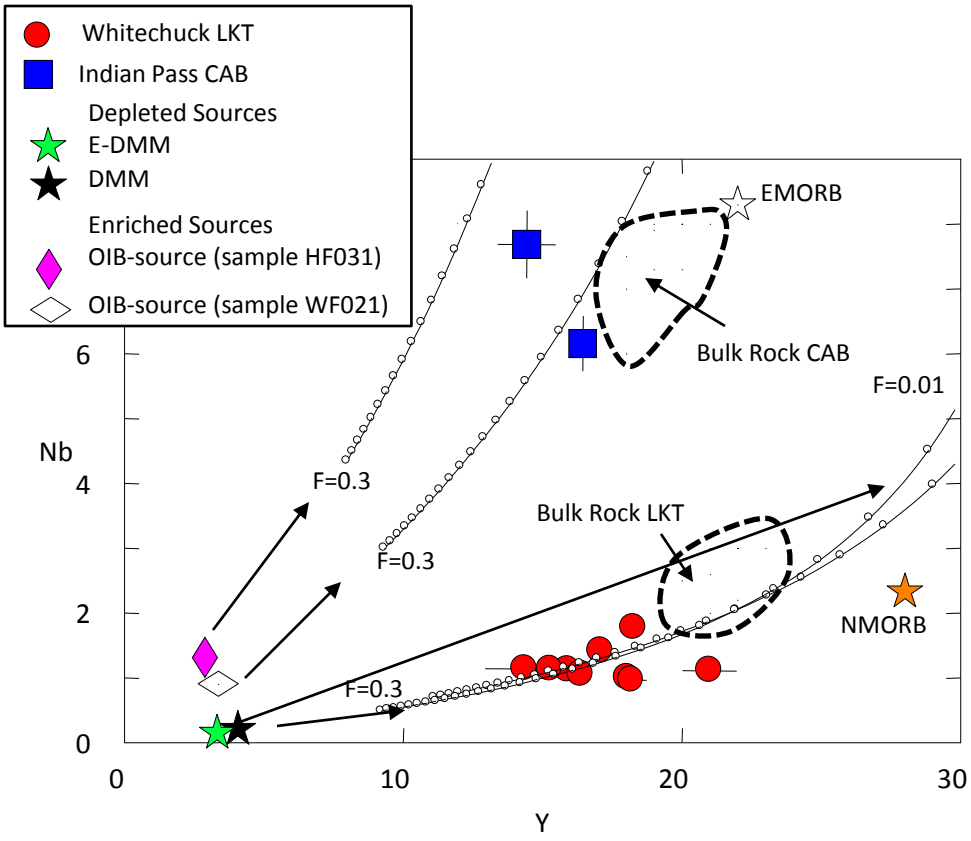

Figure 17: Nb vs.Y batch melting curves for four potential sources (diamonds and green and black stars), plotted in increments of 0.01 melt fraction (F), from 0.01 to 0.3. Trace elements from melt inclusions, corrected to mantle values (red circles and blue squares). Whole rock fields (dashed lines) show for comparison. NMORB and EMORB from Sun and McDonough (1989). E-DMM from Workman and Hart (2005). DMM from Salters and Stracke (2004). OIB sources from Ruscitto et. al (2010b). Bulk rock data from DeBari et al. (submitted).

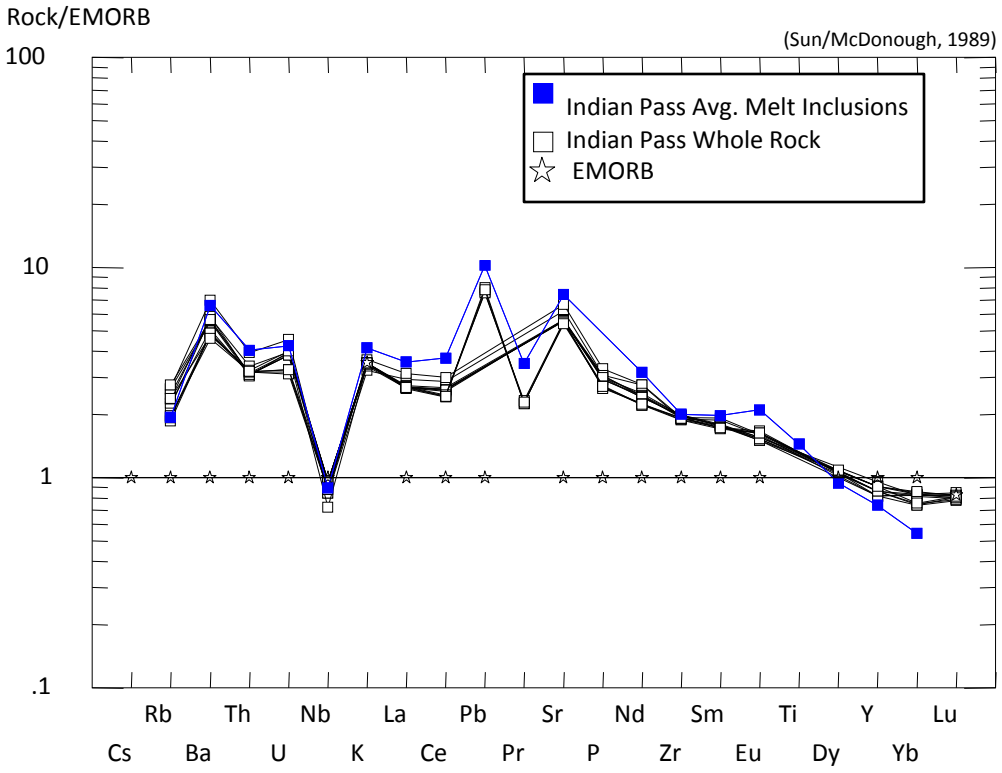

Figure 18: EMORB-normalized trace elements from average corrected Indian Pass melt inclusions (blue squares) and from whole rock concentrations (white squares) of DeBari et al. (submitted). EMORB (white stars) from Sun and McDonough (1989).

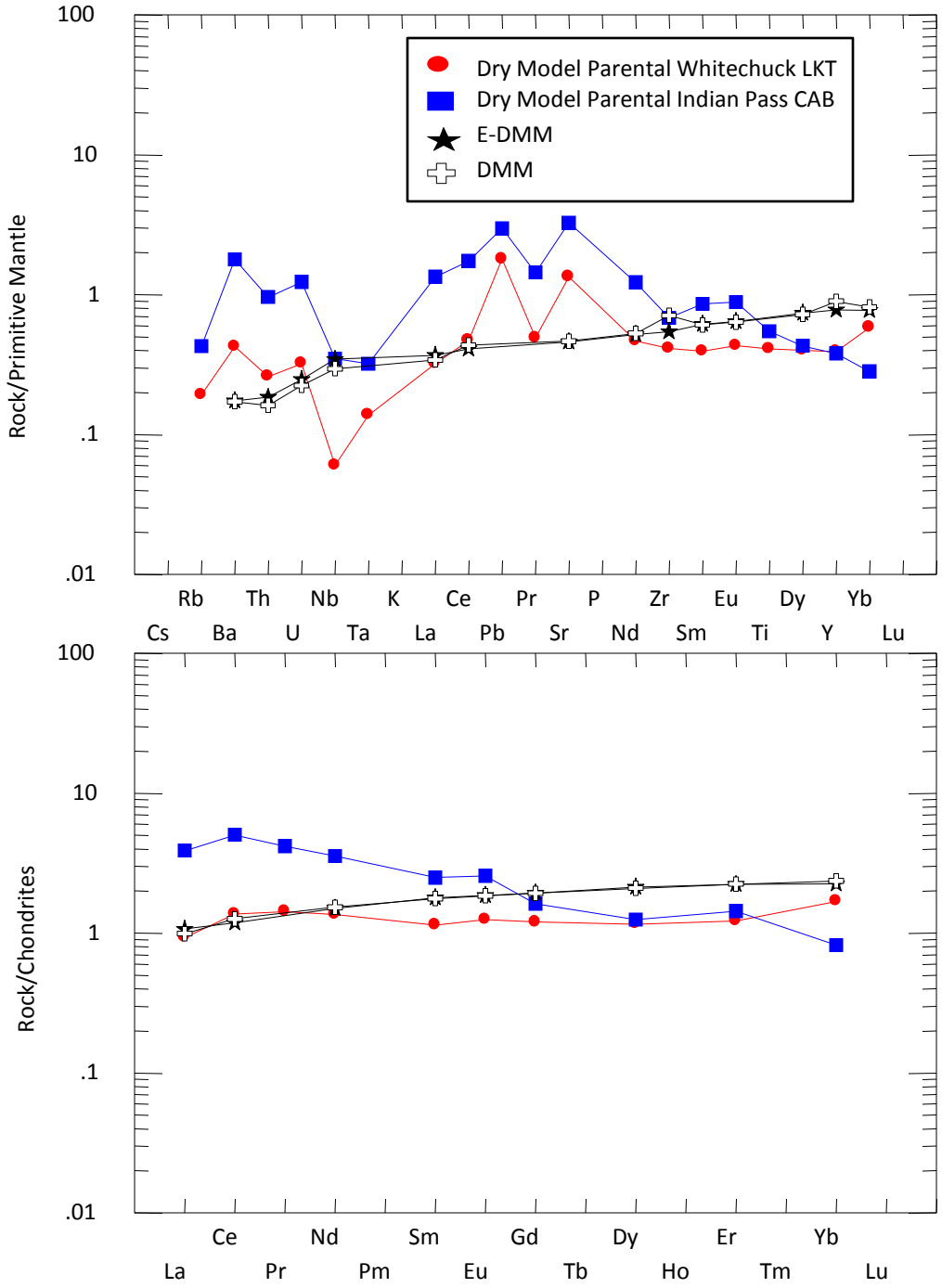

Figure 19: Modeled trace element and REE patterns of potential mantle sources, for Whitechuck LKT (red circles) and Indian Pass CAB (blue squares) normalized to chondrite (Sun and McDonough, 1989) assuming maximum dry decompression of mantle with no hydrous phases (3.8 % partial melting for LKT, 3.5% partial melting for CAB). Conserved elements (Ti, Nb, Y, Yb) are more depleted than DMM (white crosses) (Salters and Stracke, 2004) or E-DMM (black stars) (Workman and Hart , 2005).

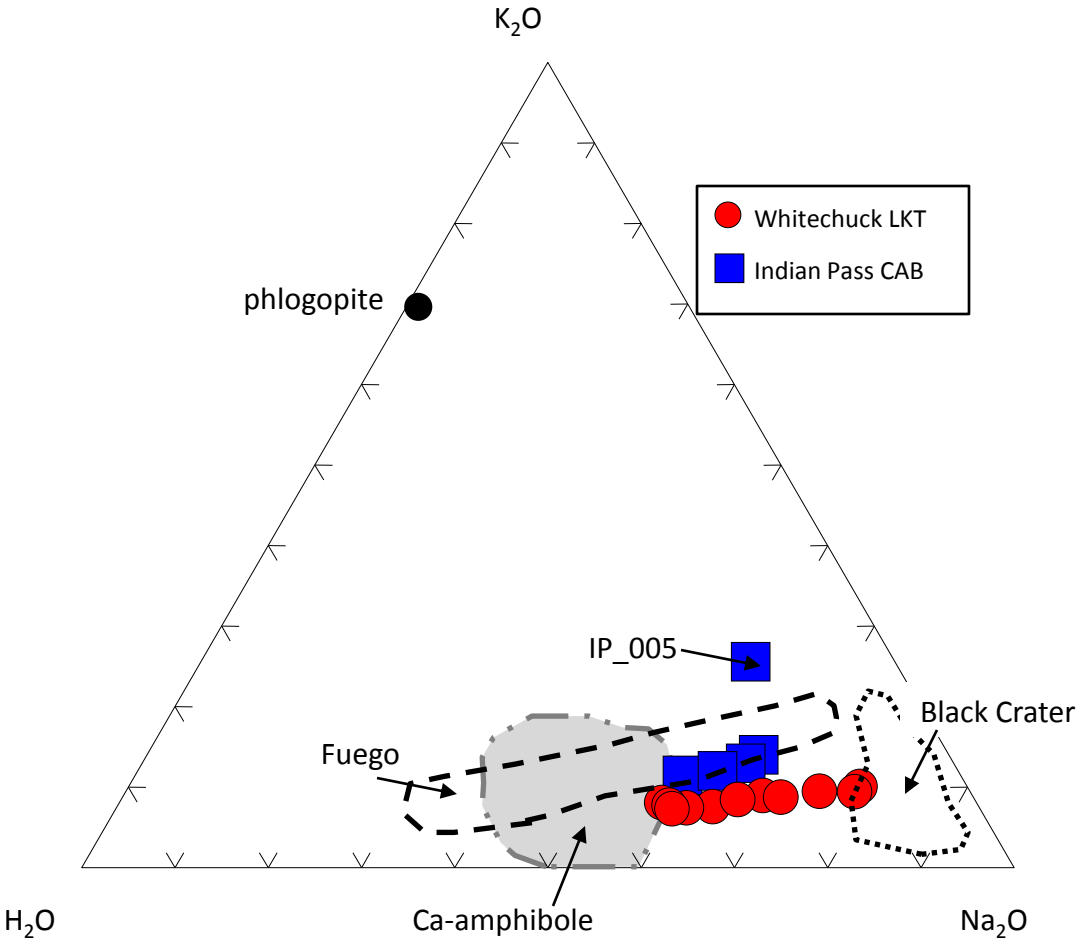

Figure 20: Comparison of alkalis and H_2O for corrected inclusions (filled symbols). Both Whitechuck and Indian Pass lavas have low amounts of K_2O, yet higher amounts of H_2O (and Na_2O). Anomalous inclusion (IP_005) is more evolved (Figs. 5, 6) and shows evidence for significant degassing (Figure 13) . Plotted fields for Black Crater (decompression (dry) source example) and Fuego (fluid-flux (wet) source example) from Sisson and Layne (1993).